UNIVERSITAT POLITÈCNICA DE CATALUNYA
BARCELONATECH
Escola Superior d'Enginyeries Industrial,
Aeroespacial i Audiovisual de Terrassa

Study: Numerical Simulations of Synthetic Jets

Degree: **Grau en Enginyeria en Vehicles Aeroespacials**

Student: **Carlos Martínez Segarra**

Director: **Arnau Miró Jané**

Co-Director: **Manel Soria Guerrero**

Delivery Date: **June 2020**

Content: **Report**

Declaració d'Honor

I declare that,

the work in this Degree Thesis is completely my own work,

no part of this Degree Thesis is taken from other people's work without giving them credit,

all references have been clearly cited,

I'm authorised to make use of the research group related information I'm providing in this document.

I understand that an infringement of this declaration leaves me subject to the foreseen disciplinary actions by The Universitat Politècnica de Catalunya - BarcelonaTECH.

Carlos Martínez Segarra		29/06/2020
Student Name	Signature	Date

Title of the Thesis : Study: Numerical Simulations of Synthetic Jets

Acknowledgement

I would like to express my gratitude to Universitat Politècnica de Catalunya for giving me access to the Juno cluster to perform my numerical simulations and to store my archives there. Thanks to such support, I have been able to perform a decent numerical analysis of synthetic jets.

I would also like to thank my director, Arnau Miró, for teaching me everything about synthetic jets and giving me access to papers and documentation which are key for the proper development of the present dissertation. He has also given me access to MareNostrum to perform some of my simulations, which is such an honor for me. I would also like to thank him for answering my doubts and questions seven days a week.

Abstract

A synthetic jet is formed by the oscillating movement of a membrane located inside a cavity. Such movement allows ambient fluid to be dragged inside and outside, hence producing a jet that is able to transfer both linear momentum and kinetic energy into the system without any external mass flux. It offers multiple interesting applications, the most relevant being active flow control and thermal control of electronic devices.

This work focuses on the study of a discharge of a slotted synthetic jet actuator into an opened external medium. Numerical simulations using Large Eddy Simulations have been performed to analyze the jet behavior and vortex dynamics. Three mesh densities and two different cases based on the SJA governing parameters have been evaluated during the analysis.

This study reveals that the advected vortex pair reaches a higher altitude before becoming the jet as the jet formation criteria becomes greater. This causes a bigger gradient on turbulent kinetic energy at higher altitudes which is closely related to the distance from the actuator orifice in which the vortex pair starts coalescing into the jet. Vortex penetration also increases with the jet formation criteria as such parameter is directly related to the actuator membrane deflection. A bigger jet formation criteria allows the membrane to deflect more, hence more fluid is dragged downstream resulting in the increase of the linear momentum contribution to the system. Such phenomenon straightaway affects the jet half-width which also increases with the jet formation criteria. This study also reveals that both cases share the same potential core which suggests that the ingestion and expulsion dynamics of a synthetic jet are independent of the jet formation criteria.

Index

List of Figures

List of Tables

1. Introduction

This chapter firstly presents the aim of the study. The next step is to justify why the topic chosen is relevant and why it has been selected. Following, the scope of this project is explained where it is specified what is included and excluded from the analysis. The requirements are also presented in order to know what is needed to successfully complete the study. There is also a state of the art section where synthetic jets are described briefly, highlighting the case where they discharge into an external quiescent medium. Finally, some of synthetic jets main applications are outlined.

1.1 Aim

The aim of this thesis is to perform numerical simulations of a synthetic jet actuator (SJA) discharging into an external quiescent medium, in order to analyze its behavior.

The focus of this project is on the evaluation of the external flow of a synthetic jet actuator. In order to achieve such goal, wall-resolved large eddy simulations (LESs) are carried out using the Wall-Adapting Local Eddy-viscosity (WALE) sub-grid scale model. The Arbitrary Lagrangian-Eulerian (ALE) formulation is used to account for the periodic movement of the SJA membrane.

Among the various existent geometries of a SJA, this work focuses on the slotted configuration. One of the main SJA governing numbers, the JFC, is evaluated throughout the span of the project. Two values of the jet formation criteria are tested: $JFC = 3$ for Case 1 and $JFC = 6$ for Case 2. The Reynolds number is set to $Re = 500$ for all the simulations.

1.2 Justification

Synthetic jets have emerged as an interesting option to do research on. The zero net mass flux condition is one of the main advantages that characterizes this actuators. Moreover, the diverse applications that feature synthetic jets, including active flow control, presents

such actuators as an appealing field for research. Synthetic jets have been selected in this project for such reasons.

The present thesis is developed within Universitat Politècnica de Catalunya and has the objective, within the possibilities and resources available, to study synthetic jets and their behavior. The study consists in performing numerical simulations in order to analyze the behavior of a SJA, for the slotted configuration, by means of analyzing the effect of the jet formation criteria on the flow. Various mesh densities are studied in order to suit the scope of this work.

1.3 Scope

The present work focuses on the analysis of the external flow coming out from a synthetic jet, in its slotted configuration, into a quiescent medium. Any other SJA configuration is not within the scope of this thesis.

Throughout the span of this work, there is also the need to create computational grids in order to later perform the CFD (Computational Fluid Dynamics) analysis. Three mesh densities (600,000 CV, 1.5 million CV and 5 million CV) are analyzed in order to deduce which is the most suitable is within the scope of this work. The final chosen mesh shall be selected as a compromise between precision and computational time. Furthermore, a basic grid convergence study is carried out between the computational grids, however, an in depth convergence study is out of the scope of this project.

The flow modeling in this analysis is performed with Alya, a high performance CFD code developed by Barcelona Supercomputing Center (BSC). The present study performs a wall-resolved large eddy simulations (LES). Reynolds-averaged Navier-Stokes (RANS) or direct numerical simulations (DNS) are out of the scope.

Once the numerical simulations are finished, data analysis and post-processing are carried out. Therefore, the development of post-processing codes in order to compute the required parameters is part of the scope of this work. Finally, experimental analysis are out of the scope of the present dissertation.

1.4 Requirements

The first step within this work is to deploy the necessary software. The meshing process is performed with software from ANSYS, ICEM CFD. Furthermore, ParaView is required for post-processing and data visualization. Matlab is also needed in order to plot the results obtained.

The behaviour of a synthetic jet is explained by means of a set of governing parameters, hence, a proper mathematical model must be adopted to compute them.

Afterwards, it is required to elaborate a literature review in order to better comprehend the behavior of synthetic jets and, hence, what to expect from the outcomes of the numerical simulations.

The CFD analysis of this work is performed in Alya. Consequently, proper setups for the numerical simulations must be prepared. These simulations are performed with two different values of the jet formation criteria ($JFC = 3$ and 6) in order to understand the behaviour of the external flow coming out of the orifice. The Reynolds number is set to 500 in all the studied cases.

The last important requirement to take into account is that this work has to be performed under four months. Therefore, the mesh density is adapted in order to obtain a mesh that is a compromise between accuracy and computational time.

1.5 State of the Art

The very first studies on synthetic jets were conducted in the 50s decade of the last century. A synthetic jet actuator (SJA) consists of a sealed cavity containing a piezoelectric membrane (or diaphragm) inside that is subjected to a time-periodic motion. The deflection of the membrane allows to expel fluid outside the cavity through the actuator orifice into the external medium [1], therefore, a determinate volume of fluid is moved downstream. A vortex pair is advected downstream until, under certain conditions, it is too far to be ingested back and, thus, a jet is formed. The rest of the fluid is ingested back into the cavity, during the ingestion phase, hence, no mass flow is added during the process. That is the reason why synthetic jets are also known as Zero Net Mass Flux (ZNMF) actuators.

Smith and Glezer [1] researched on the formation and evolution of synthetic jets. They introduced the concept of stroke length L_0 , which is the time of discharge or half the period τ of the membrane motion. It is defined as the integral of the stream-wise velocity at the exit of the orifice $u_0(t)$ during the expulsion phase (half of the membrane cycle):

$$L_0 = \int_0^{\frac{\tau}{2}} u_0(t)\, dt \tag{1.1}$$

Integrating Equation 1.1 it is possible to calculate the average orifice velocity:

$$U_0 = \frac{L_0}{\tau} \tag{1.2}$$

Smith and Glezer found that the flow at the exit medium, in the vicinity of the orifice, tends to form a pair of vortices that are advected downstream, transitioning into turbulence, until they dissipate and the jet is formed. They also found that the mean trajectories of the vortex pair at a given formation frequency scale with the stroke length L_0 , regardless from the magnitude of the formation impulse. Cater and Soria [2] later concluded that the dimensionless stroke length, L_0/d, where d is the orifice diameter, is one of the key parameters that describe the SJA flow at the exit, which is the inverse of the Strouhal Sr number:

$$\frac{1}{Sr} = \frac{L_0}{d} \tag{1.3}$$

Holman *et al.* [3] proposed a criteria for synthetic jets in order to quantify its formation, know as the jet formation criteria (JFC), which is defined in Equation 1.4:

$$JFC = \frac{1}{\overline{Sr}} = \frac{\overline{Re}}{\overline{Sk^2}} \tag{1.4}$$

where Sr is the Strouhal number, Re is the Reynolds number and Sk denotes the Stokes number. The overline operator ($\bar{.}$) indicates that these dimensionless numbers are based

on a time-and-space-averaged velocity $\overline{U}$ at the exit of the actuator during the expulsion phase ($\overline{U} = 2U_0$). The difference between the dimensionless stroke length proposed by Cater and Soria [2] and the JFC suggested by Holman *et al.* [3] is a constant value, which is further analyzed during Chapter 2.

There are different configurations for the actuator. The most important configurations are the axisymmetric and the slotted, which is the one studied in this work. The slotted configuration, as previously mentioned, allows the formation of a vortex pair in the orifice lips. This pair is formed within a viscous fluid when a force is exerted to a determinate volume of fluid, hence producing a roll-up process [4], which is further examined in Section 4.1. The roll-up allows the formation of a pair of vortices by advection with a trailing jet located behind. At a given height, which is linked to the value of the JFC, the vortical structure begins to lose its coherence and transitions into turbulence. The jet gets formed as the structure dissipates [5]. The vortex pair presents a peculiarity which is the fact that vortex separation from the trailing jet happens at a higher stroke ratio than on vortex rings [4], which are present on SJA with the axisymmetric orifice configuration. The pair of vortices is supplied with fluid coming from the trailing jet and the vorticity increases linearly with time. The pair accumulates much of the vorticity of the system while the rest is kept by the trailing jet. The behavior of a SJA discharging into an external medium is further studied during Chapter 4.

On the other side, the axisymmetric orifice configuration presents a similar behavior, though featuring vortex rings instead of vortex pairs. The vortex rings are formed at the orifice lips and are advected downstream. It is a straight three dimensional flow compared to the slotted configuration, which can be simplified to a two dimensional flow. The appearance of vortical ring-shaped structures is found in nature, e.g, in the eruption of a volcano or in the jet propulsion of some aquatic animals such as a squid or salp [6].

The membrane shape has been modeled as a sinusoidal function of the membrane radius, like Xia and Qin [7] and is further discussed during Chapter 2. Furthermore, there are four relevant instants during the phase, which begins at $\phi = 0°$ and finishes at $\phi = 360°$. The first important moment is when $\phi = 0°$, which corresponds to the maximum expulsion phase. At this point, the velocity at the orifice is the maximum at the exit medium. The next important instant within the cycle is when $\phi = 180°$, which is the maximum ingestion instant. It is the point where the velocity is the maximum inside the cavity. Another

remarkable instant is $\phi = 90°$, which corresponds to the maximum positive deflection of the membrane. It is the end of the expulsion cycle and the beginning of the ingestion phase. The final relevant instant is located at $\phi = 270°$, which is the maximum negative deflection of the membrane. As opposed to $\phi = 90°$, it is the moment where the expulsion phase begins because the ingestion cycle has just finished.

The natural frequency of the actuator membrane, know as the Helmholtz frequency f_h , is also an important aspect of a synthetic jet actuator. The Helmholtz resonance is the phenomenon of air vibrating inside a cavity, as when someone blows inside an empty bottle. If such phenomenon is present in a SJA, the compressible regime is needed due to the incompressible not being able to describe precisely the fluid behavior. It has been proved experimentally and numerically that if the ratio between the drive frequency and the Helmholtz frequency is more than 0.5 ($f_0 / f_h > 0.5$), the actuator is within the compressible regime [8].

1.5.1 SJ discharging into a quiescent medium

As the study that is performed in this work is a synthetic jet discharging into a quiescent external medium, it is adequate to analyze studied from different researchers concerning the same kind of actuator.

Goldstein *et al.* [9] conducted a direct numerical simulation (DNS) in order to model an array of two-dimensional synthetic jet slots pulsing into an initially quiescent flow. The flow physics and the sensitivity to a host of flow and geometric parameters were analyzed via using virtual surfaces. In this study, jet formation was seen to be dependent on the Reynolds number whereas the Strouhal number was seen to influence the flow evolution in the external medium. The lip shape and the length of the cavity were also seen as important influences for the resulting flow. The analysis further concluded that this simulation methods could be applied to study the control of the turbulent boundary layer.

One of the first set of numerical simulations that included an accurate model of the jet cavity was carried out by Mittal *et al.* [10]. The simulations were in two dimensions and included a Cartesian grid-based immersed boundary method that allowed computing complex moving boundaries. The outcomes from this study indicated that the vortex pair, which is formed at the orifice lips, as aforementioned, is expelled or ingested back into the cavity depending on the operational parameters of the jet. Moreover, the formation of a

jet, according to Mittal *et al.* [10], seemed to depend on parameters such as the jet frequency, velocity, orifice size and possibly fluid viscosity. According to Mittal *et al.* [10], the vortex pairs are expelled if the self-inducted velocity of the pair itself is bigger than the jet ingestion velocity.

Utturkar *et al.* [11] performed a detailed two-dimensional computational study using the same solver as Mittal *et al.* The sensitivity of the jet to the design of the jet cavity was analyzed by changing the cavity aspect ratio and the location of the oscillatory diaphragm. It was demonstrated that jet formation depends on the dimensionless stroke length, which is equal to the inverse of the Strouhal number (See Equation 1.3). Another conclusion extracted from the study is that wide-ranging changes in the cavity design have a limited effect on the jet expelled from the cavity, hence, the jet flow may be accurately modeled without an accurate cavity design, which has been disputed in future studies [12].

Holman *et al.* [3] further refined the jet formation criteria proposed by Utturkar *et al.* [11] in 2003. They evaluated a constant, K, which depends on geometric factors like the orifice shape, radius of curvature and the aspect ratio of the orifice. They stated that the dimensionless stroke length or the inverse Sr (or Re / Sk^2, as in Equation 1.4) has to be bigger than the constant K in order for jet formation to occur. The constant K is approximately $K = 1$ for the slotted configuration and $K = 0.16$ for the axisymmetric configuration. Another conclusion from this study is that vortex strength and celerity are all governed by the jet Strouhal number Sr.

Kotapati *et al.* [13] elaborated a numerical study of a transitional synthetic jet in quiescent external flow using three dimensional direct numerical simulations (DNS). This experiment attempted to model the configuration used by Yao *et al.* [14], which is shown in Figure 1.1, with a simpler representation of the cavity and orifice geometry and diaphragm placement.

One of the results derived from such study, also seen in Mittal *et al.* [10], is that the near field is characterized by the formation of vortex pairs (ring-shaped) at the lips of the orifice, which are expelled in the stream-wise direction away from the jet exit. According to Mittal *et al.* [10], such vortex pairs are expelled if the self-inducted velocity of the pair itself is bigger than the jet ingestion velocity. At the surroundings of such main pairs of vortices, rib-shaped vortical structures oriented in the stream-wise direction are also observed. These structures tend to amplify themselves quickly, producing a transformation

of the primary vortex pair into a proper turbulent jet. Furthermore, counter-rotating vortices are formed inside the cavity, during the ingestion phase, while the flow also transitions into turbulence. Kotapati *et al.* support the idea outlined by Goldstein *et al.* [9], Utturkar *et al.* [11] and Holman *et al.* [3] that the Strouhal number is a key parameter in order to describe the behavior of the jet flow. They demonstrated that the vortex trajectory and celerity are primarily determined by the Sr number. Kotapati *et al.* also conclude that the cavity details, within an incompressible regime, do not alter significantly the behavior of the external jet flow.

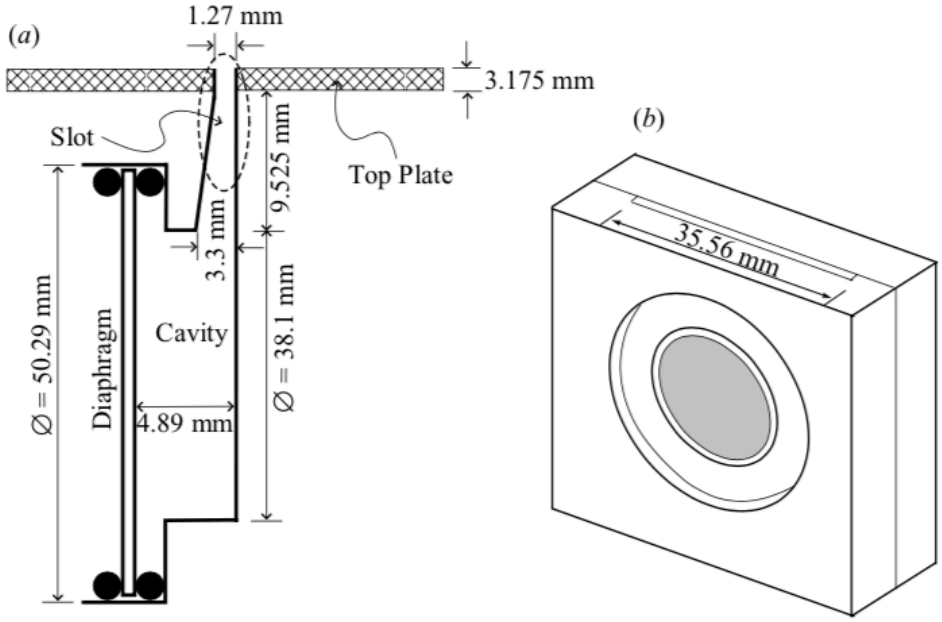

FIGURE 1.1 : Configuration used by Yao *et al.* [14]

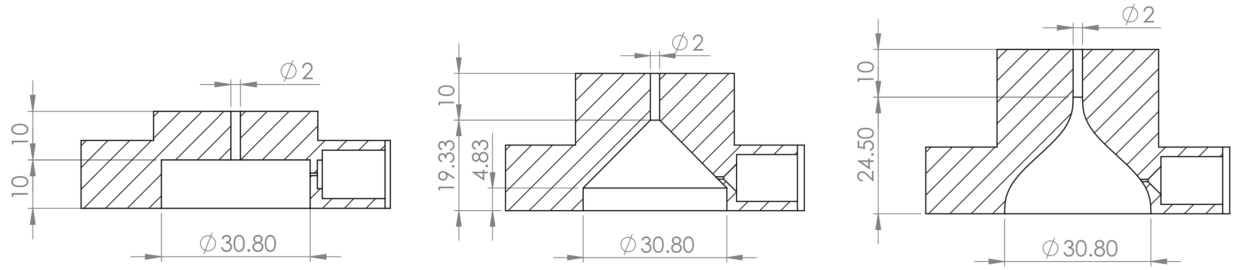

(a) Cylindrical (S1) (b) Conical (S2) (c) Contraction (S3)

FIGURE 1.2 : The three different axisymmetric shaped cavities used by Feero *et al.* [12]

Feero *et al.* [12] conducted an experiment in order to study the effect of the cavity shape on synthetic jets. In their analysis, synthetic jets parameters, such as cavity volume or orifice diameter, are kept constant throughout the comparison of the three axisymmetric SJA with different shapes each. The three different shape cavities that were tested,

cylindrical, conical and contraction, are shown in Figure 1.2. The cavity pressure and velocity at the orifice exit are measured in this experiment near the Helmholtz resonance of the cavity. The radial velocity profiles appeared to be different in the three orifice shapes. Furthermore, both the Reynolds number and the momentum flux, which is key for AFC applications, decreased sequentially from the cylindrical shaped cavity to the conical and, finally, to the contraction cavity. The final conclusion extracted from this work is that synthetic jet performance is dependent on the cavity shape up to a certain degree.

1.5.2 Synthetic Jet Applications

Synthetic jets have been object to many studies. Due to their behavior and advantages, researchers have opted out to explore in which fields can synthetic jets be applied. This section presents a brief outline of the main ones.

1.5.2.1 Active Flow Control

The most notable application for synthetic jet actuators is related to the active control of a flow field (AFC). It is a relevant application within the aerospace industry in order to decrease drag while the lift is increased, hence improving the aerodynamic efficiency. The way to achieve such result is by introducing kinetic energy in the boundary layer.

An important parameter when AFC is analyzed is the momentum coefficient. It is defined as follows:

$$C_\mu = \frac{n{U_0}^2 S_d}{{U_\infty}^2 S_\infty} \tag{1.5}$$

where U_0 is the the average orifice velocity, U_∞ is the velocity of the external flow, n is the number of synthetic jets used , S_d is the orifice area and S_∞ is the characteristic area.

During the 60s of the last century, it was demonstrated that the use of steady blowing or suction allowed to increase the lift and to reduce the drag, although the plumbing system needed was difficult to implement. One of the first simulations with a blowing and suction AFC device was performed by Spalart *et al.* [15]. The goal was to unload the wind of a V-22 tilt-rotor aircraft via a Detached-Eddy Simulation using a modified NACA 0012.

Following authors used synthetic jets as active flow control devices. In this regard, Tuck and Soria [16] experimented on active flow control with a SJA in a NACA 0015 airfoil. They used a two dimensional airfoil in a water tunnel to perform their experiments. One of the results both researchers found in their experiment was the stall angle of attack diminished from 10 degrees to 18. The result was a 46% increase in the maximum lift coefficient of the airfoil. Those lift improvements were due to a generation of a row of lifting vortices, in the span-wise direction, which convected over the suction surface of the airfoil, therefore allowing the flow field to remain attached to the upper part of the airfoil for more angles of attack.

McCormick [17] developed the directed synthetic jet, which is analogous to a synthetic jet but its neck is curved instead of straight. Such geometry is implemented in order to energize the boundary layer flowing over the orifice by dragging the fluid (with low momentum) via suction on the in-stroke and by blowing the fluid (with high momentum) on the out-stroke. Therefore, the flow separation is shown to be avoided. By using such device it is possible to prevent flow separation without taking into account external flow parameters.

More recently, Rodriguez *et al.* [18] studied the actuation on the boundary layer of a SD7003 airfoil at $Re = 6\ x\ 10^4$ using a synthetic jet actuator. Large Eddy Simulations were performed in this analysis. This study focused on a particular range of low Re numbers where the development of Micro Air Vehicles (MAV) is of interest. At such low Reynolds numbers and low angles of attack a laminar separation bubble (LSB) appears and hinders its aerodynamic efficiency. Increasing the angle of attack allows the appearance of LSB bursting and, hence, stall is produced. The aim of this work was to improve aerodynamic efficiency on these conditions. They were able to cancel the LSB bursting at angle of attack $AoA = 4^o$, although aerodynamic efficiency in the airfoil was not improved. Another important finding for the actuation developed was that it allowed to remove the flow separation at angles of attack above the maximum lift point, resulting in a net aerodynamic efficiency of 124% and a 46% reduction of the C_D.

1.5.2.2 Other SJA Applications

Another interesting application of a SJA is related with the thermal control of small electronic devices. The main target within this application is to cool any tiny electronic part down in order to boost its performance and to improve its life span (reliability).

In this regard, Arshad *et al.* [19] studied synthetic jet actuators for heat transfer enhancement. They showed that the vortices expelled form the orifice penetrate the thermal boundary layer on a heated surface, thus, increasing the turbulence on that surface and achieving the heat transfer adequately. As a SJA is easy to implement and handle, according to Arshad *et al.*, it allows to reduce the cost of the thermal management system.

Miró [5] analyzed the flow and heat transfer of impinging synthetic jets. The axisymmetric and slotted configurations were studied and compared. It was revealed that the axisymmetric configuration reaches a higher heat transfer peak than the slotted, although heat transfer diminishes faster for the axisymmetric compared to the slotted when moving away from the jet centerline. This can be an important point to keep in mind when implementing a thermal control device with a SJA: each configuration has its pros and its flaws depending on the requirements of the thermal control device.

Another application where synthetic jets have been proved to be capable is as a propulsion mechanism for small autonomous underwater vehicles (AUV). The concept behind this application is to mimic the pulsatile jet propulsion of some sea animals, like jellyfish, skid or salp. Polsenberg et al. [6] used a genetic algorithm technique in order to optimize the actuation profile of the thrusters from their SJA prototypes. This group of researchers conclude reporting synthetic jets are a viable solution as a way of propulsion for small autonomous underwater vehicles.

2. Mathematical and Numerical Development

The second chapter of this dissertation presents a mathematical and numerical model for a SJA. Firstly, the slotted configuration, which is the one adopted in this analysis, is presented with the actual values of the dimensionless parameters needed in order to set the case. The next step within this chapter is to mathematically develop the Navier-Stokes equations needed to describe the behavior of a synthetic jet actuator. Afterwards, the model needed to represent the actuator membrane movement is shown. Finally, the dimensionless governing parameters such as the Reynolds number (Re), the Stokes number (Sk) and the Strouhal (Sr) number are explained.

2.1 SJA Configuration Studied

The synthetic jet actuator configuration used in this numerical study is the slotted one (see Figure 2.1).

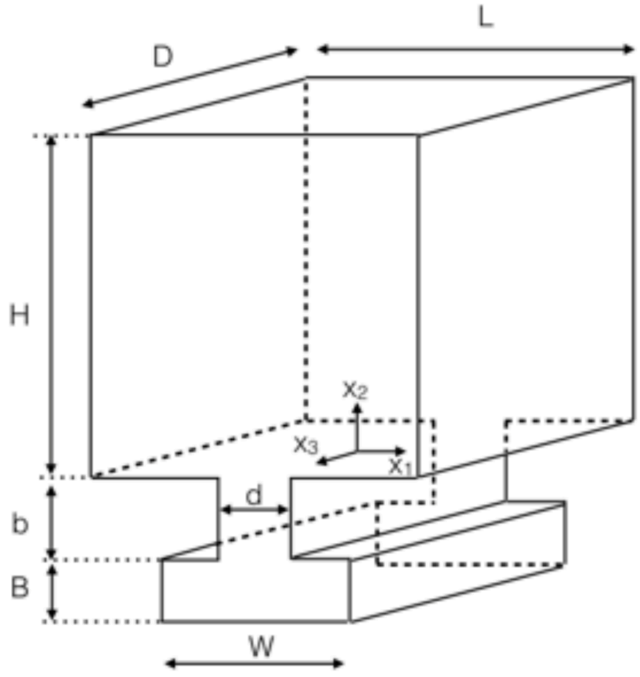

FIGURE 2.1 : The Slotted Configuration used in this study. (Not to scale)
Extracted from [5].

The domain exit is represented by a tetrahedron whose dimensions are $L\ x\ H\ x\ D$. The cavity is, as well, displayed as a tetrahedron and the actual dimensions of it are $W\ x\ B\ x\ D$. This configuration also presents a tetrahedron-shaped neck, or orifice, that connects the cavity with the external medium whose dimensions are $d\ x\ b\ x\ D$. There is a membrane or diaphragm inside the actuator that oscillates with a determined frequency, hence, producing the jet. As one of the aims of this study is to see how the jet evolves when it is in the external medium, the top wall of the domain of study is located at an orifice to surface ratio of $H/d = 60$, which is considered far enough to allow jet propagation.. The relation between the width of the external medium domain and the orifice exit diameter L/d is set to 60, in order to let the jet evolve within the external medium. The depth (in the x_3 direction) to orifice exit diameter ratio (D/d) is set to 6, as in Miró [5] and Kotapati et al. [13], in order to allow the three dimensional flow to develop properly. Miró [5] set the dimensionless cavity width to $W/d = 23.5619$, so to impose a $JFC = 3$, with a mean amplitude $A/d = 0.2$, as it is further explained. The ratio between the height of the actuator channel and the orifice exit diameter is fixed to $b/d = 1/3$, as Miró [5] and Liu [20] did.

	W/d	**H/d**	**L/d**	**B/d**	**b/d**	**D/d**
Case 1 & 2	23.5619	60	60	4.1888	1/3	6

TABLE 2.1 : The dimensions used for the slotted configuration for both cases studied.

The next step is to determine the value for the height of the cavity B. Miró [5] used $JFC = 3$ for his simulations. Figure 2.2 shows the ratio between the height of the cavity and the orifice exit diameter $\delta c/B$ for JFC = 0-10 used by Miró. According to the figure, for $JFC = 3$ the ratio $\delta c/B$ is 0.1885, which means the deflection of the membrane is 18.85% of the cavity height. Bigger deflections are unrealistic and issues may occur when applying the ALE model if considered. Therefore, the chosen height of the cavity, B, is bigger than the one selected by Miró ($B = 5/3$). Figure 2.3 presents the ratio between the height of the cavity and the orifice exit diameter $\delta c/B$ for JFC = 0-10 used in this work. It has been decided to set $\delta c/B = 0.15$ for $JFC = 6$, which is the maximum JFC studied and, therefore, the cavity height is set to $B = 4.1888$. A 15% maximum deflection for the membrane in relation to the cavity height is a safe value, considering that Miró used 18.85% for his analysis. Setting $\delta c/B = 0.15$ also leaves room to increase the JFC (e.g.

$JFC = 9$) for future works. The values used for the slotted configuration for both cases studied in this work are summarized in Table 2.1 .

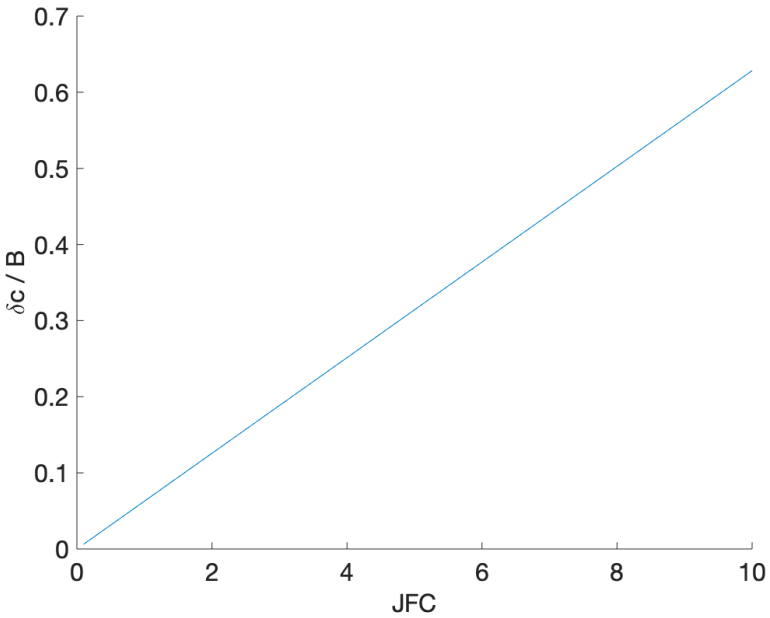

FIGURE 2.2 : The ratio between the height of the cavity and the orifice exit diameter $\delta c/B$ for $JFC = 0$-10 used by Miró [5].

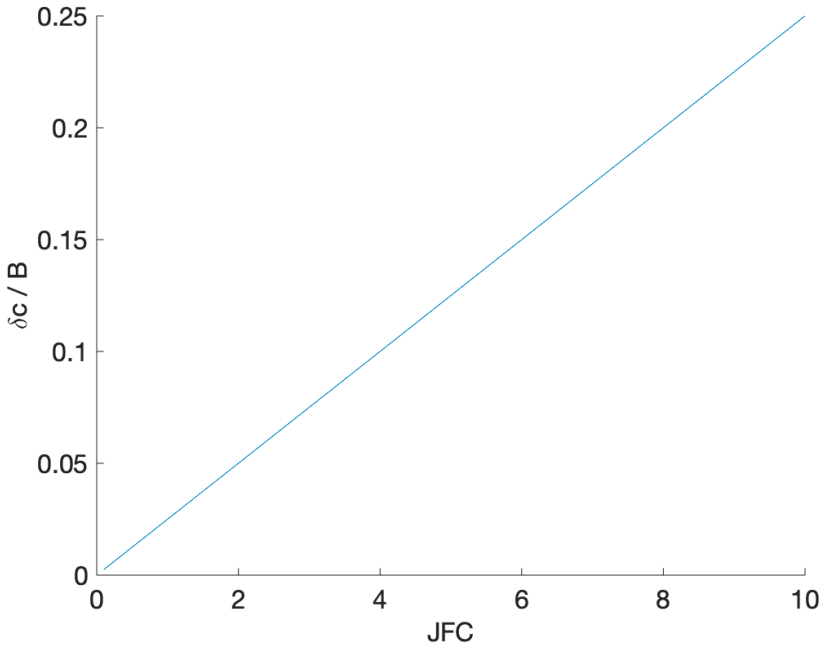

FIGURE 2.3 : The ratio between the height of the cavity and the orifice exit diameter $\delta c/B$ for $JFC = 0$-10 used in this work in order to obtain the value of B .

The Helmholtz frequency, as aforementioned the actuator's natural frequency, can be described with the following formula [12]:

$$f_h = \frac{v_s}{2\pi}\sqrt{\frac{\omega\ d}{W\ \omega\ B\ b}} \tag{2.1}$$

where v_s is the speed of the sound within the fluid. It is possible to observe that the actuator natural frequency is proportional to the area of the cavity orifice and inversely proportional to both the neck length and cavity volume. The orifice exit diameter has been set to $d = 1\ mm$. The Reynolds number is set to $Re = 500$ for the simulations. Additionally, standard air conditions and the values from Table 2.1 are considered. It is possible to observe in Figure 2.4 that the ratio between the actuator driving frequency and the Helmholtz frequency is lower than $f_0\ /\ f_h < 0.5$ for $JFC = 3$ and $JFC = 6$, which are both cases studied in this work. Therefore, the incompressible regime is considered.

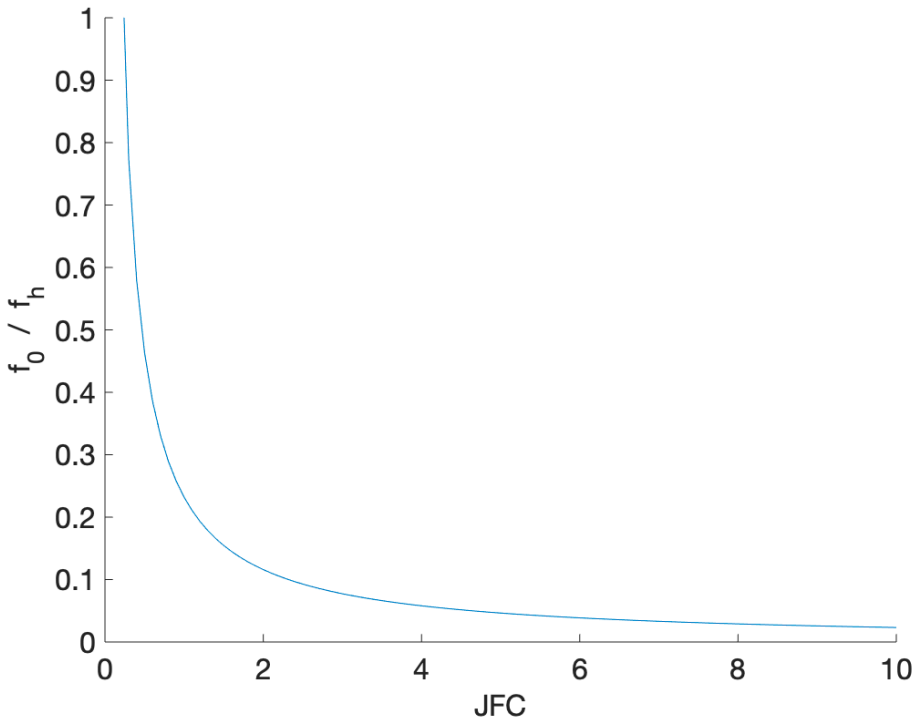

FIGURE 2.4 : The ratio between the actuator driving frequency and the Helmholtz frequency $f_0\ /\ f_h$ for JFC = 0-10.

2.2 Mathematical Development of the Governing Equations

The mathematical model used to describe the flow which is adopted for the numerical simulations of this study is based on the Navier-Stokes equations. Such set of equations are of key importance in order to characterize the physics of a flow field. The Navier-Stokes equations that are needed during the present analysis are the continuity equation and the momentum conservation equation.

As it was earlier stated, the present work analyzes an incompressible case of study since the ratio between the Helmholtz actuator frequency and the driving frequency is less than 0.5. Under such hypothesis, the Navier-Stokes equations are:

$$\frac{\partial u_j}{\partial x_j} = 0 \tag{2.2}$$

$$\frac{\partial u_i}{\partial t} + \frac{\partial (u_i u_j)}{\partial x_j} = -\frac{1}{\rho}\frac{\partial p}{\partial x_i} + \frac{\partial}{\partial x_j}\left[\nu\left(\frac{\partial u_i}{\partial x_j} + \frac{\partial u_j}{\partial x_i}\right)\right] \tag{2.3}$$

where:

· x_i are the spatial coordinates $[m]$.

· u_i are the velocity components $\left[\frac{m}{s}\right]$.

· p is the pressure $\left[\frac{N}{m^2}\right]$.

· T is the temperature $[K]$.

· ρ is the density $\left[\frac{kg}{m^3}\right]$.

· ν is the kinematic viscosity $\left[\frac{m^2}{s}\right]$.

· t is the time $[s]$.

2.2.1 Dimensional Analysis of the Continuity Equation

The Navier-Stokes equation of continuity has already been presented in this chapter (Equation 2.2). Some dimensionless magnitudes need to be defined in order to perform the proper dimensional analysis. Moreover, this dimensionless numbers are defined from two characteristic parameters of the synthetic jet configuration used in this study. In this case, the characteristic velocity U_0 and the orifice exit diameter d are used:

$$\hat{u}_j = \frac{u_j}{U_0} \; ; \qquad \hat{x}_j = \frac{x_j}{d}$$

The hat above the velocity $\hat{u}_j$ and the coordinate $\hat{x}_j$ means both parameters are dimensionless. For the sake of simplicity, both equations are reorganized as follows:

$$u_j = \hat{u}_j U_o \; ; \qquad x_j = \hat{x}_j d$$

The next step within this mathematical development is to substitute both u_j and x_j into Equation 2.2:

$$\frac{\partial \hat{u}_j}{\partial \hat{x}_j} \frac{U_0}{d} = 0 \tag{2.4}$$

The above equation can be further simplified if it is taken into account that any term multiplied by zero in an equation is zero. Finally, Equation 2.5 is obtained as the dimensionless form of the Navier-Stokes continuity equation needed for the numerical study of this project:

$$\frac{\partial \hat{u}_j}{\partial \hat{x}_j} = 0 \tag{2.5}$$

2.2.2 Dimensional Analysis of the Momentum Conservation Equation

The Navier-Stokes equation of momentum conservation has already been presented in this chapter (Equation 2.3). Similarly to the continuity equation case, some dimensionless parameters have to be established in order to perform the dimensional analysis later. In order to define such dimensionless magnitudes, some characteristic parameters from the adopted synthetic jet configuration are needed. Apart from the characteristic velocity U_0 and the orifice exit diameter d which were already adopted in the development of the continuity equation, the membrane oscillating frequency f_0 is also used. Both the velocity $\hat{u}_i$ and the coordinate $\hat{x}_i$ have an analogous development as $\hat{u}_j$ and $\hat{x}_j$, hence, they are not presented. The dimensionless magnitudes needed to continue the development are the following :

$$\hat{t} = 2\pi f_0 t \; ; \qquad \hat{p} = \frac{p}{\rho {U_0}^2}$$

Aiming to simplify the process t and p are isolated from each equation resulting in:

$$t = \frac{\hat{t}}{2\pi f_0} \; ; \qquad p = \hat{p}\rho {U_0}^2$$

The following step consists in the substitution of the four variables defined above into Equation 2.7. After applying all substitutions the equation is as follows:

$$\frac{\partial \hat{u}_i}{\partial \hat{t}} 2\pi f_0 U_0 + \hat{u}_j U_0 \frac{\partial \hat{u}_i}{\partial \hat{x}_j} \frac{U_0}{d} = -\frac{1}{\rho} \frac{\partial \hat{p}}{\partial \hat{x}_i} \frac{\rho {U_0}^2}{d} + \frac{\partial}{\partial \hat{x}_j d} \left[\nu \left(\frac{\partial \hat{u}_i}{\partial \hat{x}_j} \frac{U_0}{d} + \frac{\partial \hat{u}_j}{\partial \hat{x}_i} \frac{U_0}{d} \right) \right] \qquad (2.6)$$

The next part of the development is to further simplify Equation 2.6. The density disappears from the right hand side of the equation. If both sides of the equation are multiplied by $\frac{d}{{U_0}^2}$, the equation is reorganized as:

$$\frac{\partial \hat{u}_i}{\partial \hat{t}} \frac{2\pi f_0 d}{U_0} + \hat{u}_j \frac{\partial \hat{u}_i}{\partial \hat{x}_j} = -\frac{\partial \hat{p}}{\partial \hat{x}_i} + \frac{\partial}{\partial \hat{x}_j} \left[\frac{\nu}{U_0 d} \left(\frac{\partial \hat{u}_i}{\partial \hat{x}_j} + \frac{\partial \hat{u}_j}{\partial \hat{x}_i} \right) \right] \tag{2.7}$$

After these steps, there are two dimensionless numbers emerging from this equation, as already stated in [1]. Both numbers are the Reynolds number and the Strouhal number, which are defined as follows:

$$Re = \frac{U_0 d}{\nu} \tag{2.8}$$

$$Sr = \frac{2\pi f_0 d}{U_0} \tag{2.9}$$

Consequently, Equation 2.7 is transformed into:

$$\frac{\partial \hat{u}_i}{\partial \hat{t}} Sr + \hat{u}_j \frac{\partial \hat{u}_i}{\partial \hat{x}_j} = -\frac{\partial \hat{p}}{\partial \hat{x}_i} + \frac{\partial}{\partial \hat{x}_j} \left[\frac{1}{Re} \left(\frac{\partial \hat{u}_i}{\partial \hat{x}_j} + \frac{\partial \hat{u}_j}{\partial \hat{x}_i} \right) \right] \tag{2.10}$$

Equation 2.10 results as the dimensionless form of the momentum conservation equation which is used according to the configuration set for this project.

Both equations needed to define the mathematical model that describes the flow field of a synthetic jet have been developed and found. The final form of this equations is:

$$\frac{\partial \hat{u}_j}{\partial \hat{x}_j} = 0 \tag{2.11}$$

$$\frac{\partial \hat{u}_i}{\partial \hat{t}} Sr + \hat{u}_j \frac{\partial \hat{u}_i}{\partial \hat{x}_j} = -\frac{\partial \hat{p}}{\partial \hat{x}_i} + \frac{\partial}{\partial \hat{x}_j} \left[\frac{1}{Re} \left(\frac{\partial \hat{u}_i}{\partial \hat{x}_j} + \frac{\partial \hat{u}_j}{\partial \hat{x}_i} \right) \right] \tag{2.12}$$

2.3 Actuator Membrane Model

The membrane in a synthetic jet actuator is a key element of the system that produces the periodic motion that allows to form the jet flow. The membrane motion is modeled in Xia and Qin [7] and Miró *et al.* [5] using a time-dependent sinusoidal function and a space-dependent profile function $\delta(x)$, as follows:

$$y = -\delta(x)\ cos(2\pi f_0 t) \tag{2.13}$$

where x represents the orifice diameter at time t. The membrane shape is modeled with the parameter $\delta(x)$. There are different models used for such parameter but the proposition used by Xia and Qin [7] and Miró *et al.* [5] is an efficient approximation as well as simple. The membrane shape of the synthetic jet actuator in this study is modeled as a cosine function of the membrane radius, as it can be seen in Equation 2.14:

$$\delta(x) = \delta_C\ cos(\pi \frac{r}{W}) \tag{2.14}$$

Another important parameter to define the behavior of the synthetic jet is the mean amplitude, as it is further explained in this chapter. The mean actuator amplitude is defined as follows:

$$\bar{A} = \frac{1}{S_W} \int_{S_W} \delta(x)\ dS \tag{2.15}$$

where S_W is the actuator membrane surface. An expression for δ_C can be obtained by integrating the mean actuator amplitude equation (Equation 2.15) analytically. The resultant membrane shape is calculated as follows:

$$\delta_C = \frac{\pi}{2} \bar{A} \tag{2.16}$$

which allows to compute δ_C in a simple manner.

In order to compute the velocity profile at the orifice, taking into account the incompressible regime and assuming continuity between the orifice and the membrane, the following expression is obtained:

$$\int_{S_d} u_2(x,z,t)\ dS = \int_{S_W} \frac{\partial y}{\partial t}\ dS \tag{2.17}$$

where $u_2(x,z,t)$ is the velocity profile at the orifice lips. If the integral is solved by using the expression from Equation 2.15 (note that the integral only affects the term that describes the shape), the resultant expression is as follows:

$$\int_{S_d} \delta_2(x)\ dS = S_W \bar{A} \tag{2.18}$$

where $\delta_2(x)$ is the profile function for $u_2(x,z,t)$ when a similar function to the one in Equation 2.13 is used. Mimicking the approach used in Equation 2.15:

$$\bar{A_2} = \frac{S_w}{S_d}\bar{A} \tag{2.19}$$

where $\bar{A_2}$ is the mean amplitude of the profile. Equation 2.19 relates the increase that the orifice amplitude needs, with such increase being the ratio between the geometry at the actuator cavity and the geometry at the actuator neck. Taking into account that for a constant profile,

$$u_2(t) = 2\pi f_0 \frac{S_w}{S_d}\bar{A} sin(2\pi f_0 t) \tag{2.20}$$

where $u_2(t)$ is the velocity at the orifice.

2.4 Analysis of the Governing Parameters

This section presents the implementation of the actuator model developed in Section 2.3 into the mathematical model developed in Section 2.2. In Chapter 1, Equation 1.2 defined the average orifice velocity, in terms of the period, while it can also be defined in terms of the actuator frequency f_0 ($U_0 = L_o f_0$). The stroke length is already defined in Equation 1.1 as follows

$$L_0 = \int_0^{\frac{\tau}{2}} u_0(t)\ dt \tag{2.21}$$

where $u_0(t)$ is the stream-wise velocity at the exit of the orifice during the expulsion phase (half of the actuation period). Therefore, U_0 can be defines as follows:

$$U_0 = \frac{1}{\tau}\int_0^{\frac{\tau}{2}} u_0(t)\ dt \tag{2.22}$$

A first approximation stated that $u_0(t)$ presented a slug shape [1] whereas, later [21], it was assumed that it is more precise to define $u_0(t)$ using the space-averaged velocity at the exit, as it can be seen in Equation 2.23:

$$u_0(t) = \frac{1}{S_d}\int_{S_d} u_2(x,z,t)\ dS \tag{2.23}$$

where S_d is the exit orifice surface and $u_2(x,z,t)$ is the velocity at the orifice lips. Therefore:

$$U_0 = \frac{1}{\tau}\frac{1}{S_d}\int_0^{\frac{\tau}{2}}\int_{S_d} u_2(x,z,t)\ dS\ dt \tag{2.24}$$

Equation 2.24 can also be expressed as an time-and-space-averaged velocity $\overline{U}$ at the exit of the actuator during the expulsion cycle, as follows:

$$\overline{U} = \frac{2}{\tau}\frac{1}{S_d}\int_0^{\frac{\tau}{2}}\int_{S_d} u_2(x,z,t)\; dS\; dt \tag{2.25}$$

where S_d is, as aforementioned, the exit orifice surface. The relation between both characteristic velocities is $\overline{U} = 2U_0$, as it can be deduced from Equations 2.24 and 2.25. If Equation 2.25 is considered, then the Stokes number is defined as:

$$Sk = \sqrt{\frac{2\pi f d^2}{\nu}} \tag{2.26}$$

and it can be used to characterize the flow, as it is done with the Strouhal number.

The jet formation criteria equation used in Chapter 1 (Equation 1.4) was defined using the characteristic velocity from Equation 2.25, $\overline{U}$, for both Reynolds and Strouhal numbers as follows:

$$JFC = \frac{1}{Sr(\overline{U})} = \frac{Re(\overline{U})}{Sk^2} = \frac{2Re}{Sk^2} \tag{2.27}$$

The relation between the dimensionless stroke length L_0/d and the JFC is proven to be:

$$JFC = \frac{1}{\pi}\frac{L_0}{d} \tag{2.28}$$

hence, the constant $1/\pi$ is the only difference between the JFC and the dimensionless stroke length, as indicated by Miró [5].

As aforementioned in Section 2.3, the membrane vertical position can be modeled using Equation 2.13 to compute its position with the proposition used in Equation 2.14. If the time derivative is performed to Equation 2.13, the instantaneous velocity at the actuator membrane is found:

$$\frac{dy}{dt} = 2\pi f_0 \delta(x)\ sin(2\pi f_0 t) \tag{2.29}$$

As the case is under incompressible conditions, by continuity, the velocity at the orifice exit has to be the same as the velocity at the actuator membrane, as follows:

$$\int_{S_d} u_2(x,z,t)\ dS = \int_{S_W} 2\pi f_0 \delta(x)\ sin(2\pi f_0 t)\ dS \tag{2.30}$$

The only term which is affected by the integral at the right side of the equation is $\delta(x)$. If the definition of mean amplitude is recalled from Equation 2.15, the following expression is deduced:

$$\int_{S_d} u_2(x,z,t)\ dS = 2\pi f_0 \overline{A} S_W\ sin(2\pi f_0 t) \tag{2.31}$$

Equation 2.31 can be substituted inside Equation 2.24, as follows:

$$U_0 = \frac{1}{\tau}\frac{S_W}{S_d}\int_0^{\frac{\tau}{2}} 2\pi f_0 \overline{A}\ sin(2\pi f_0 t)\ dt \tag{2.32}$$

If the time integral is applied to Equation 2.32, the result is the following:

$$U_0 = 2\overline{A} f_0 \frac{S_W}{S_d} \tag{2.33}$$

Expression 2.33 shows that the characteristic velocity U_0 depends on the mean amplitude and the driving frequency f_0.

If Equation 2.33 is substituted in the definitions of the Reynolds number and the Strouhal number that have been presented earlier in this chapter (Equations 2.8 and 2.9), the result is as follows:

$$Re = \frac{2\overline{A} f_0 d}{\nu} \frac{S_W}{S_d} \tag{2.34}$$

$$Sr = \pi \left(\frac{d}{\overline{A}} \right) \left(\frac{S_d}{S_W} \right) \tag{2.35}$$

As it is demonstrated by Miró [5], the JFC becomes a pure geometrical parameter:

$$JFC = \frac{2}{\pi} \left(\frac{\overline{A}}{d} \right) \left(\frac{S_W}{S_d} \right) \tag{2.36}$$

As concluded by Smith and Glezer [1] and Miró [5], the formation parameters of the jet only depend on the mean amplitude of the actuator.

Equation 2.36 shows that the way to modify the JFC is by changing the $\overline{A}/d$ term. The mean amplitude has been set to $A/d = 0.2$ for the $JFC = 3$ case, as Miró [5] in his analysis. Since the $JFC = 6$ case is also studied in this work, according to Equation 2.36, the way to obtain such increase in the JFC is by setting the mean amplitude to $A/d = 0.4$.

3. Case of study

This chapter presents the case of study that is used in the numerical simulations. Afterwards, there is a section where the case geometry and the mesh construction are explained. The next step is to present the boundary conditions which are applied to the walls and exits of the domain. The setup used to perform the simulations is also presented in this chapter. Finally, a mesh and grid sensitivity analysis is also addressed, where the different meshes used for the study are compared.

There are several parameters which characterize the behavior of a SJA, e.g., the Reynolds number, Re. This work aims to study the changes in the jet formation criteria, JFC, hence, two different cases are evaluated in this analysis: Case 1, with $JFC = 3$, and Case 2, with $JFC = 6$. Table 3.1 presents both cases studied and the most significant parameters from each of them. All geometrical parameters introduced in Table 2.1 for the slotted configuration are the same for both cases, except for the A/d. The mean amplitude, A/d, is set to $A/d = 0.2$ for Case 1 and to $A/d = 0.4$ for Case 2, as explained in Section 2.4. The Stokes number for both cases is determined using Equation 2.26. The frequency for each case is set using the aforementioned Equation 2.1. A summary of the most important parameters used in this work for both cases is presented in Table 3.1

	JFC	**Re**	**Sk**	**Freq. [Hz]**	**A/d**
Case 1	3	500	18.2574	0.02653	0.2
Case 2	6	500	12.9099	0.05305	0.4

TABLE 3.1 : Both cases studied in this work and its characteristic parameters.

3.1 Geometry and Mesh Construction

The geometry employed in this work has been adapted from Miró *et al.* [5, 22]. The main difference in the present work is the height of the exit is $H/d = 60$. The geometry is adapted to represent the external jet by adding more divisions inside and changing the height of the exit H/d, but also changing the mesh concentration factors, which are explained in the next section.

Figure 3.1 presents the geometry used in this study and Figure 3.2 shows the neck geometry in detail. The bottom wall of the cavity is formed by the horizontal line that contains points 0, 1, 2 and 3 in the figure. On the other side, the horizontal lines formed by points 4, 5 and 6, 7 represent the top wall of the cavity. Finally, the left wall and right wall of the cavity of the SJA are formed by points 0, 4 and 3, 7, respectively.

Figure 3.2 shows the geometry of the actuator neck used in this study. The neck is shadowed in the figure in order to clearly identify it. Both neck walls are formed by the vertical lines defined by points 5, 9 and 6, 10, respectively. The two horizontal lines formed by point 5, 6 and 9, 10 respectively represent the cavity geometry where the fluid is transferred from the cavity into the external medium.

Figure 3.1 shows in detail the exit geometry of the SJA. The left wall of the exit geometry is formed by the line which contains points 8, 12, 16, 20 and 24. Likewise, the vertical line which is formed by points 11, 15, 19, 23 and 27 represents the right wall of the exit SJA geometry. The horizontal line that includes points 24, 25, 26 and 27 represents the top wall of the exit domain. The bottom wall of the exit geometry is described by two horizontal lines: the line formed by points 8 and 9 and the line formed by points 10 and 11. The three horizontal lines between the bottom wall of the domain and the top wall are placed there in order to set the mesh concentration factor better, as it is explained in Section 3.2. Likewise, the vertical lines between the left wall and right wall of the exit geometry are used to establish the mesh concentration factors.

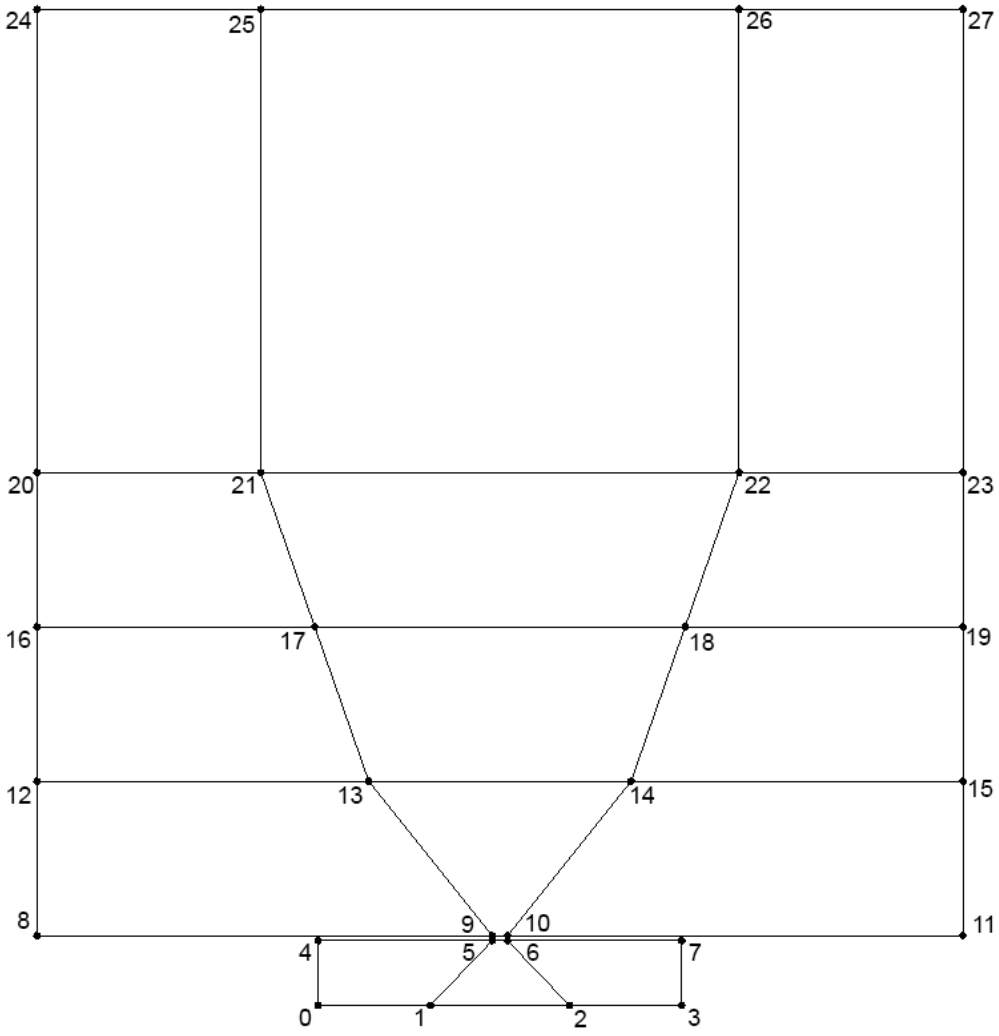

FIGURE 3.1: The geometry used for the SJA.

FIGURE 3.2: The geometry used for the orifice neck of the SJA. The neck itself is shadowed.

Once the geometry has been set, the mesh is built. Next up, there is a comparison between the three meshes studied: the first with 600,000 CV, the second with 1.5 million CV and the last with 5 million CV. The meshes have been elaborated with ICEM CFD and scripted in a python code that generates a file that can be executed in the program.

	600.000 CV	**1.5 million CV**	**5 million CV**
f_neck	6	3.8	2.5
f_act1	90	58	29
f_act2	150	120	70
f_dom1	90	65	34
f_dom2	390	320	230
f_dom3	120	100	50
f_dom4	220	160	95
f_dom5	390	320	230

TABLE 3.2 : Concentration factors used to build the three meshes studied.

First, the 2D mesh is build as shown in Figure 3.3. Subsequently, it is extruded in the z direction in order to obtain the 3D mesh that is used in the numerical simulations. In order to build the mesh, concentration factors have been assigned to the walls of the domain geometry. These concentration factors are multiplied by a differential ds, resulting in the n parameter. This parameter is the distance between two control volumes in the mesh. As the n gets bigger, there is more distance between control volumes and, hence, the mesh is less dense. On the other side, if the n has a low value, the mesh becomes much denser due to the fact that the distance between control volumes is smaller. Table 3.2 presents the concentration factors used for each of the three meshes studied. The *f_ neck* concentration factor has been designated to the four lines formed by points 5, 6, 9 and 10 of Figure 3.1. The *f_ act1* factor has been applied to the wall inside the cavity which is impinged by the vortex pair, formed by points 1 and 2. The *f_ act2* concentration factor has been assigned to the left and right walls of the cavity. The entire left wall of the exit domain and the right wall have been assigned with the *f_ dom2* factor. In order to maintain uniformity at the exits of the domain, the *f_ dom5* concentration factor applied to the top wall of the domain has the same value as the *f_ dom2*. The inner centerlines of the exit domain,

formed by points 13 and 14, 17 and 18, and 21 and 22, are designated with the concentration factors *f_ dom1*, *f_ dom3* and *f_ dom4*, respectively. The other secondary inner lines of the domain which connect two of the previously mentioned are defined with an exponential function that varies the concentration factor starting from one and exponentially increasing (or decreasing) until the other. As it can be seen in Table 3.2, the mesh is not homogenous throughout the domain. The biggest mesh density has been given to the neck, the exit of the orifice into the cavity and, most important, the exit of the orifice into the external medium, with the biggest concentration up until $y/d = 10$. These are the most relevant zones of the domain, where the analysis has been more exhaustive.

Figure 3.3 presents the three mesh densities studied in this work. Comparing the first mesh with the second, the edges of the domain, as it can be seen in Table 3.2 (*f_ dom2* and *f_ dom5*), are a bit denser but the important increase is in the exit of the orifice (*f_ dom1*) which is far more concentrated. This allows to compute better the exit of the cavity during the simulations. The difference between the second and third mesh is significant. The exit of the orifice for a higher range of y/d (*f_ dom1*, *f_ dom3* and *f_ dom4* in Table 3.2) is significantly denser than the intermediate mesh studied. There is also more density at the domain walls but it is not as remarkable as in the exit of the orifice. This increase in the number of CV allows for a way better precision in the simulations at the expense of large computational time.

Figure 3.4 shows the mesh density inside the cavity. The difference is minor if the first and the second meshes are analyzed. There is more noticeable density at the exit of the orifice (*f_ act1*) but, in the cavity walls, the mesh density is similar compared to the first. The difference between the intermediate and big mesh is significant again. The cavity is fully concentrated with the exit where the impinging wall is located particularly dense.

Figure 3.5 present the difference in mesh density among the necks of the three meshes analyzed. As the neck has been dense since the first mesh, the increase in concentration between the three meshes is not as dramatic as in the other two comparisons. The mesh density inside the neck is decent in the first mesh (*f_ neck*) and, as it can be seen in Table 3.2, the *f_ neck* factor increases at a similar ratio among the meshes.

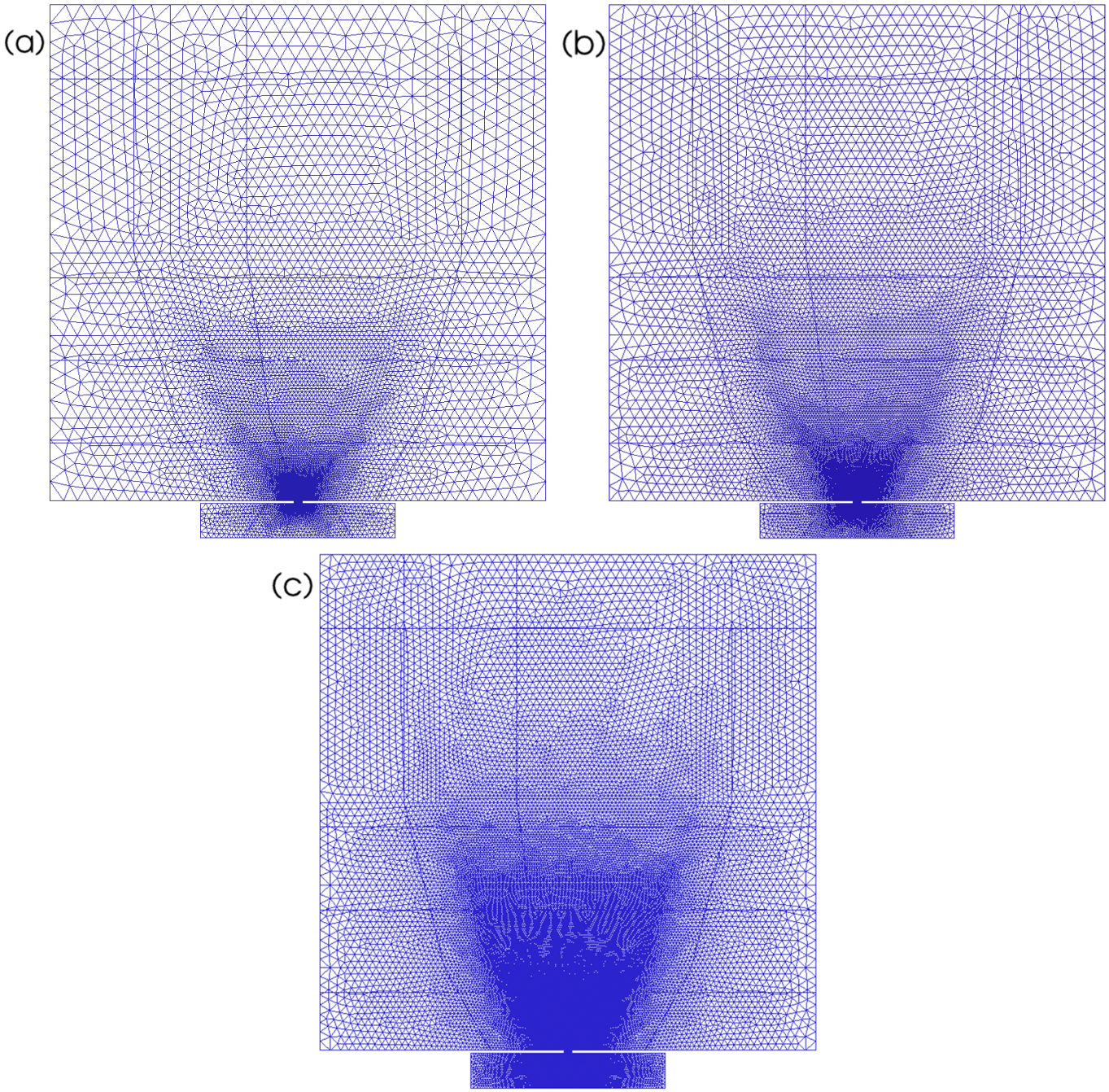

FIGURE 3.3: The three mesh densities studied in this work: (a) 600,000 CV mesh (b) 1.5 million CV mesh (c) 5 million CV mesh.

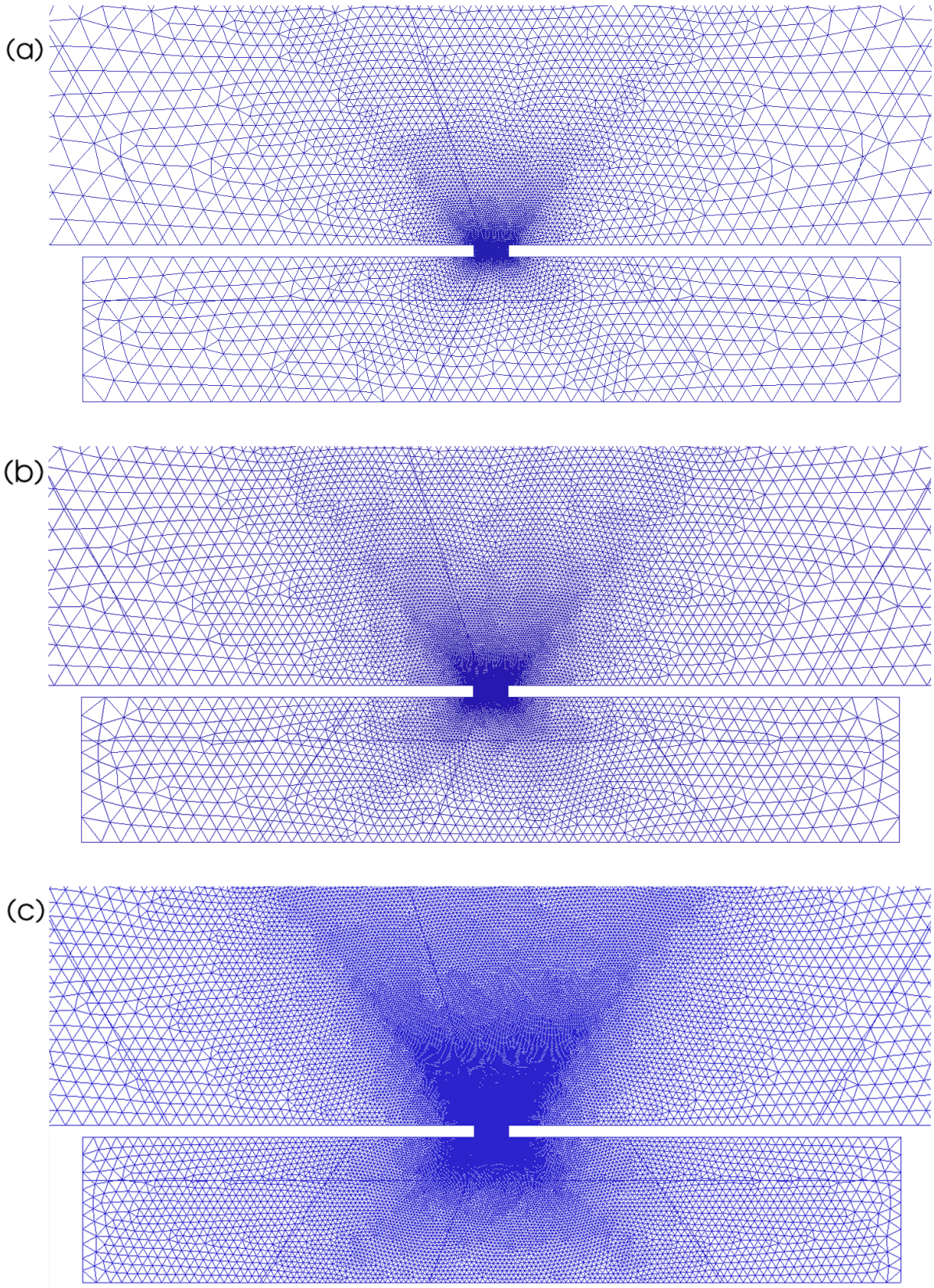

FIGURE 3.4: The mesh density inside the cavity for the three meshes studied in this work: (a) 600,000 CV mesh (b) 1.5 million CV mesh (c) 5 million CV mesh.

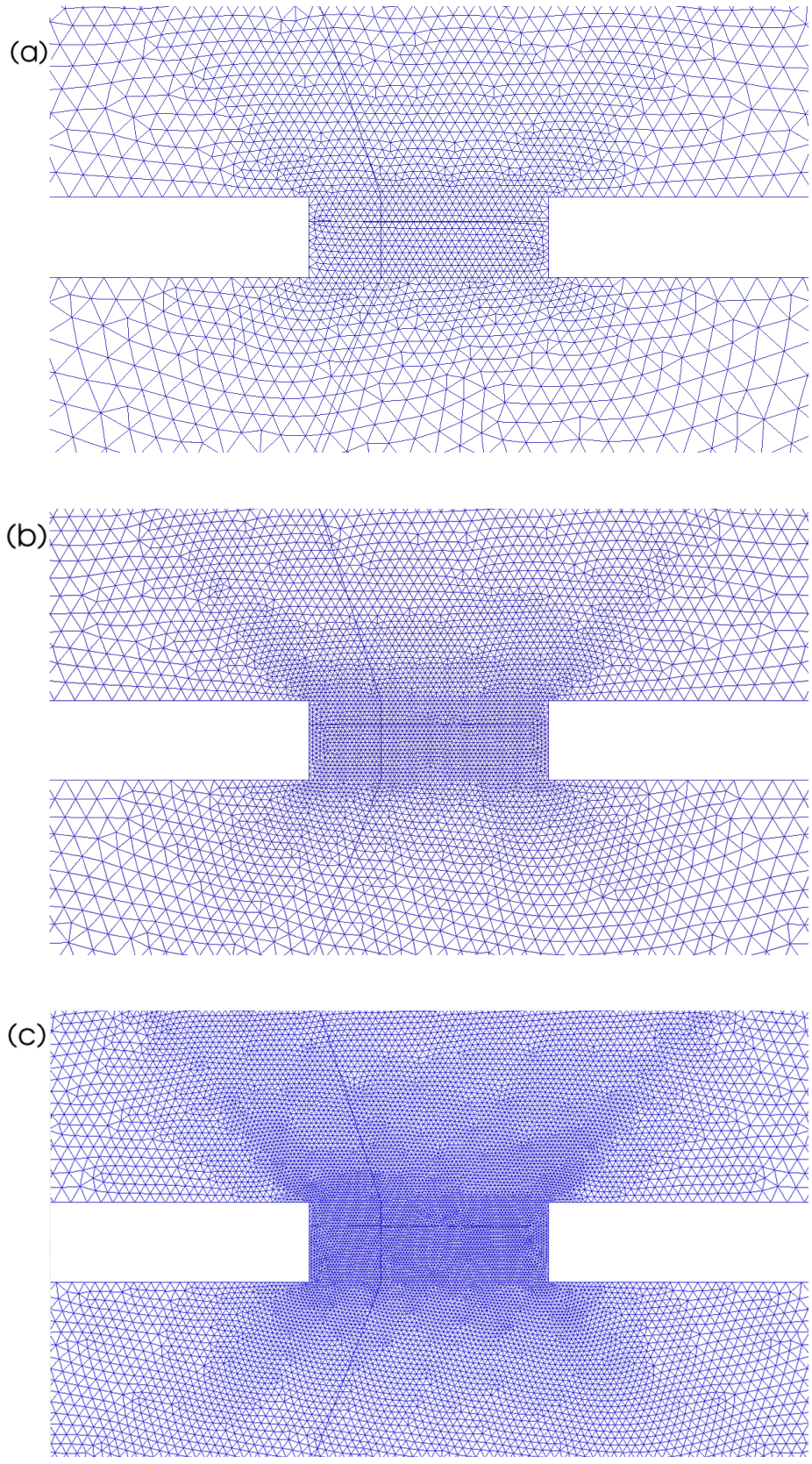

FIGURE 3.5: The mesh density in the neck for the three meshes studied in this work: (a) 600,000 CV mesh (b) 1.5 million CV mesh (c) 5 million CV mesh.

3.2 Boundary Conditions

Boundary conditions must be applied to the exit and walls of the geometry domain. They are configured in Alya. At the end of the meshing process with ICEM CFD, the patches are numbered in order for Alya to recognize them.

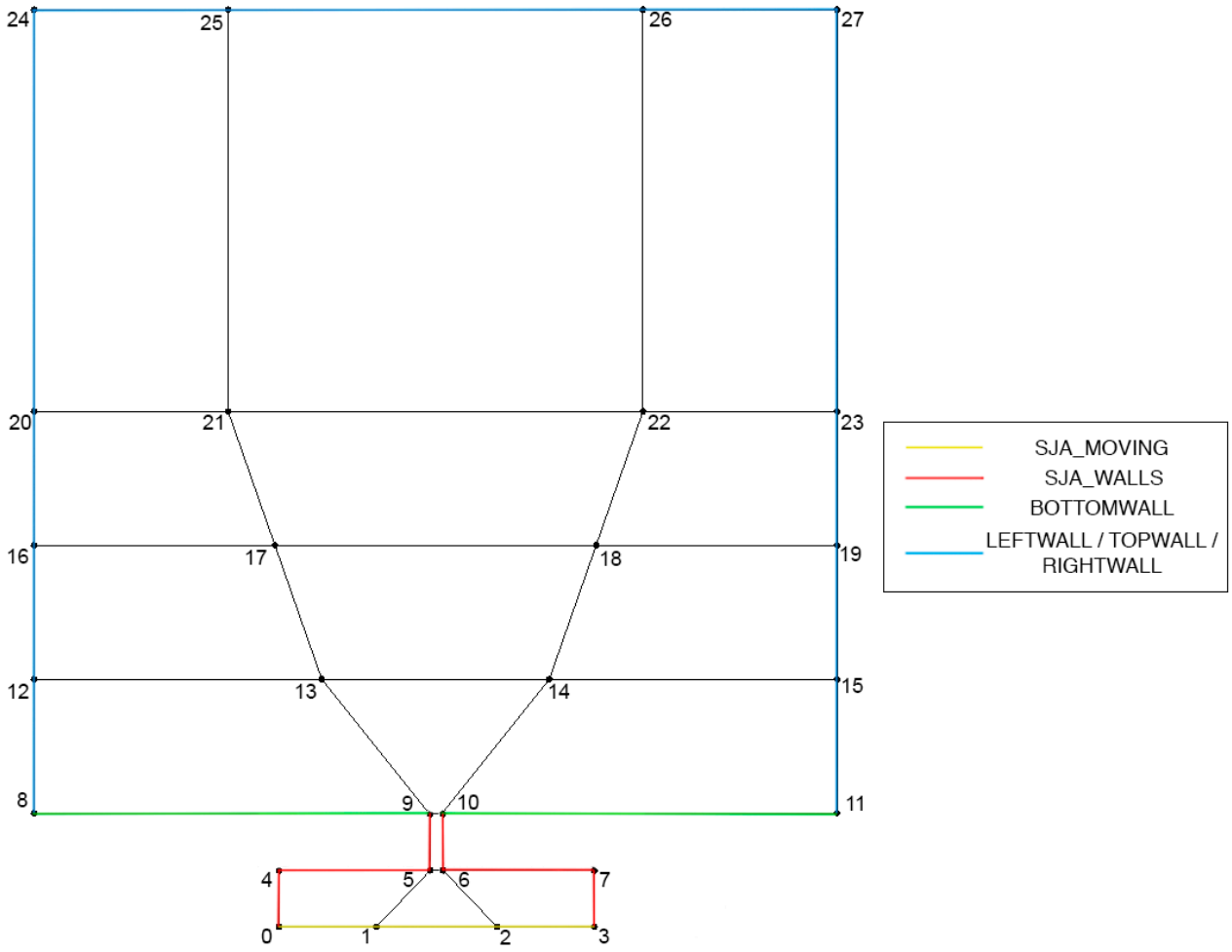

FIGURE 3.6: The boundary conditions applied to the domain of the case of study.

Figure 3.6 presents the domain geometry with the boundary conditions used to perform the simulations. It is possible to observe that the left wall of the exit domain, as well as the right wall and the top wall have the same boundary condition. It is the exit boundary condition due to the fact that this work is an open synthetic jet actuator and there are no walls in this part of the domain. The horizontal lines formed by points 8, 9 and 10, 11 represent the bottom wall of the exit domain and the wall boundary condition is assigned to them. This wall has the subtype 3 designated in order for the Alya code to distinguish each different wall of the domain. The moving membrane wall (shadowed in yellow in

Figure 3.6) is known as *SJA_MOVING* within the Alya code and it has the wall boundary condition applied with subtype 1. The other walls from the cavity and both vertical walls in the neck, represented in red, have the *SJA_WALLS* naming inside the Alya code. They have the wall boundary condition designated and subtype 2.

3.3 Alya Setup

The code used to perform the simulations in this work is Alya. Alya is a high performance mechanics code used to solve complex multi-physics problems. It is based on the Finite Element method, using a fractional step approach to solve the pressure-velocity coupling with energy conservative numerical schemes and an explicit fourth-order Runge-Kutta time integration scheme [23] coupled with an eigenvalue time step selector. The present work performs a wall-resolved large eddy simulation (LES), which has been tested in previous researches using Alya, like Miró *et al.* [24]. Alya has been developed in the Barcelona Supercomputing Center (BSC) and is designed using advanced High Performance Computing programming techniques to solve common engineering problems on supercomputers efficiently.

The mesh extracted from ICEM CFD is exported in Fensap format. The first step in the setup is to convert the Fensap file into an Alya mesh file. The alya-f2alya code has been employed for this purpose using in the following command:

```
alya-f2alya fensap.grd fensap.grd.cfg faces asc
```

where the inputs are the fensap files (.grd and .grd.cfg), whether to set the boundaries in the faces or the nodes and, finally, asc stands for ASCII (file format in which the mesh is exported).

The next step within the setup is to generate the periodicity. The code alya-selectPerNodes is handled for this aim by using the following command:

```
alya-selectPerNodes syntheticjet 0 6
```

where it is required to specify the name of the Alya case (in this example syntheticjet) and the z coordinate of the first plane ($z/d = 0$) and the z coordinate of the last plane ($z/d = 6$) have to be specified.

A strategy has been adopted [5, 22] in order to reduce the time in which the statistically stationary state is obtained, thus also reducing computational time. A precursory simulation using a coarse mesh of 300,000 CV has been run for twenty cycles in order to obtain an initial velocity map for subsequent runs. Therefore, the simulation using the 600,000 CV mesh is started with this aforementioned initial map. Likewise, it has been done with the 1.5 million mesh simulation, where the last instant of the 600,000 CV mesh simulation has been used to initialize the flow. Therefore, the next step in the Alya setup is to export the velocity field of the previous case in which the current is based. The following command is used for such purpose:

```
export_field -v VELOC -s -1 -e -1 syntheticjet.ensi.case
```

The code used is export_field. The flag -v is employed to specify the variable, in this case velocity (*VELOC*). The flags -s (start) and -e (end) are used to specify the starting and ending position of the conversion, where -1 stands for the final instant. Finally, the name of the ensight case is indicated.

Afterwards, the Alya case needs to be configured with the current initial velocity field and it is done with the following command:

```
./alya-config -c Re500.ini
```

where *Re500.ini* is the initial velocity field.

The next step is to edit the *submit_alya* file and add the number of processors used during the numerical simulation. Once it is done, the next step is to generate the initial map for the current Alya case. The code alya-ini_map is used in the following code:

```
alya-ini_map -f ../ini_map_V -o VELOC.dat syntheticjet
```

The -f flag is used to specify the initial velocity field. In this case, it is the file *ini_map_V* . The next step is to determine the output file (*VELOC.dat*) and the current case (*syntheticjet*).

The final step after all the scripts have been checked is to run the simulations. The command screen is used to open the window where the simulation is performed.

Finally, when the following command is executed,

```
. submit_alya
```

the simulation begins.

3.4 Mesh and Grid Sensitivity Analysis

In this section, the phase-averaged stream-wise V_y/U_0 velocity profiles compare the three different meshes analyzed in this work, the 600,000 CV mesh, the 1.5 million CV mesh and the 5 million CV mesh, in order to extract a conclusion on which is the most suitable mesh, taking into account the scope of this study.

Figure 3.7 presents the cross-stream distributions of phase-averaged stream-wise V_y/U_0 velocity during the maximum expulsion phase for three different stations comparing all meshes studied, the 600,00 CV mesh (blue), the 1.5 million CV mesh (red) and the 5 million CV mesh (green), for both cases: Case 1 (left) and Case 2 (right). For the first station in Case 1, the simulation performed with the 600,000 CV mesh underpredicts the 1.5 million CV mesh simulation in the region $-0.4 < x/d < 0.4$. Outside this region, the smaller mesh overpredicts the results given from the intermediate mesh simulation. At the same time, both meshes underpredict the results from the 5 million CV mesh in the area $-0.35 < x/d < 0.35$ and overpredict the 5 million CV mesh outside this region. In the other two profiles extracted from Case 1, the 600,000 CV mesh and the 1.5 million CV mesh constantly underpredict the results from the biggest mesh, except at the peak point of the curve from profile *iii*, where both meshes offer almost identical curves and underpredict the curve from the 5 million CV mesh. This is probably an indicator that mesh density is lacking from profile *iii* onwards. For Case 2, the tendency within the three profiles is that the small mesh underpredicts the results of the intermediate and big mesh in the region $-0.35 < x/d < 0.35$, whereas outside this area the 600,000 CV mesh overpredicts the results obtained with the other two simulations. The 5 million CV mesh simulation in profile *ii* of Case 2 matches the results obtained with the 1.5 million CV mesh within the zone $-0.3 < x/d < 0.3$, whereas outside this range both curves diverge slightly. Profile *iii* in Case 2 shows the exact same phenomenon in zone $-0.2 < x/d < 0.2$ and outside this area the results obtained from both meshes diverge.

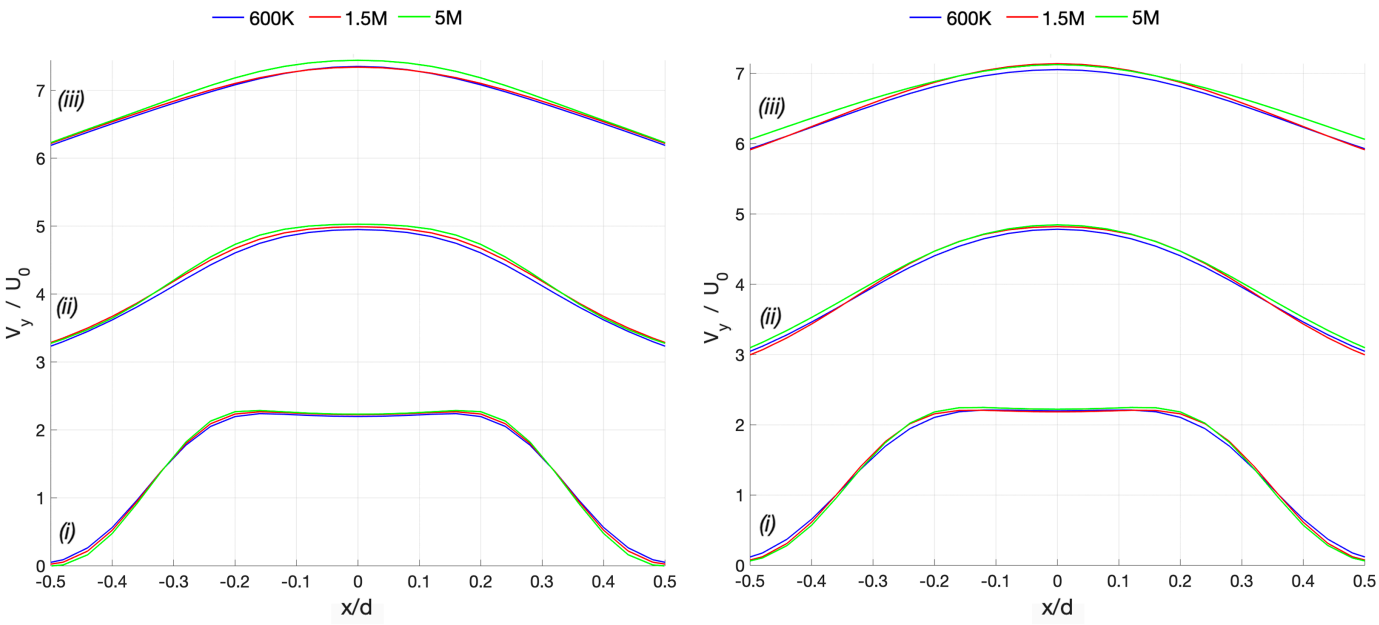

FIGURE 3.7: Cross-stream distributions of phase-averaged stream-wise V_y/U_0 velocity during the maximum expulsion phase comparing the 600,000 CV mesh, the 1.5 million CV mesh and the 5 million CV mesh for Case 1 (left) and Case 2 (right) at stations *(i)* $y/d = 0$, *(ii)* 0.5 and *(iii)* 1.

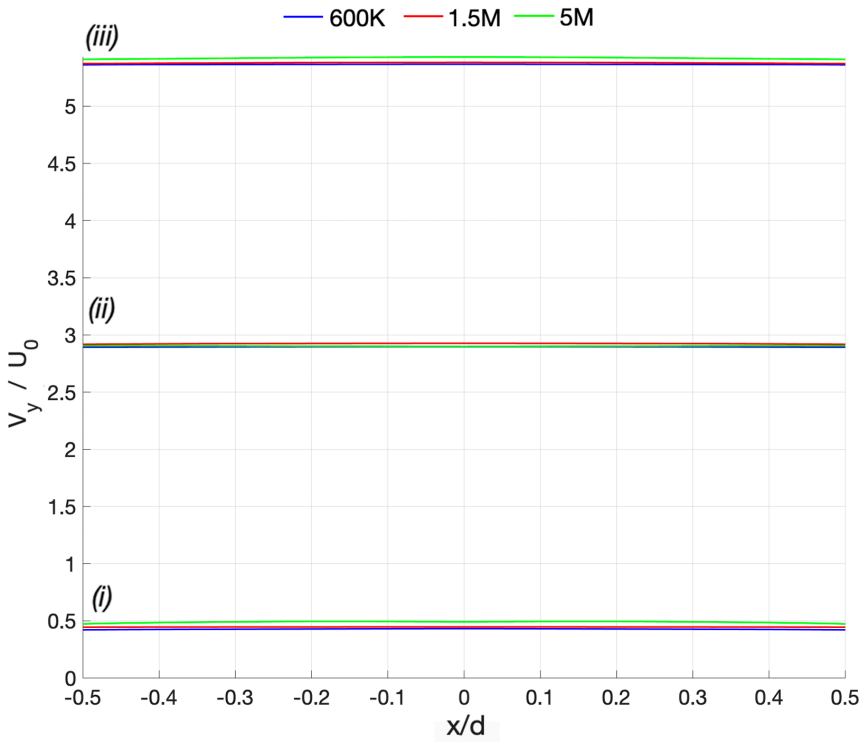

FIGURE 3.8: Cross-stream distributions of phase-averaged stream-wise V_y/U_0 velocity during the maximum expulsion phase comparing the 600,000 CV mesh, the 1.5 million CV mesh and the 5 million CV mesh for Case 1 at stations *(i)* $y/d = 10$, *(ii)* 12 and *(iii)* 14.

Figure 3.8 presents the phase-averaged stream-wise V_y/U_0 velocity profiles during the maximum expulsion phase for three higher stations (y/d = 10, 12, 14) comparing all meshes analyzed, the 600,00 CV mesh (blue), the 1.5 million CV mesh (red) and the 5 million CV mesh (green) for Case 1. At this higher stations, the small mesh and the intermediate present similar results. Nevertheless, the small mesh simulation is still underpredicting the results extracted from the 1.5 million CV mesh. Both meshes underpredict the results from the 5 million CV mesh in profiles *i* and *iii*. Nonetheless, in profile ii the curve of the bigger mesh follows a similar pattern to the smaller mesh curve, diverging slightly from the results of the intermediate mesh simulation.

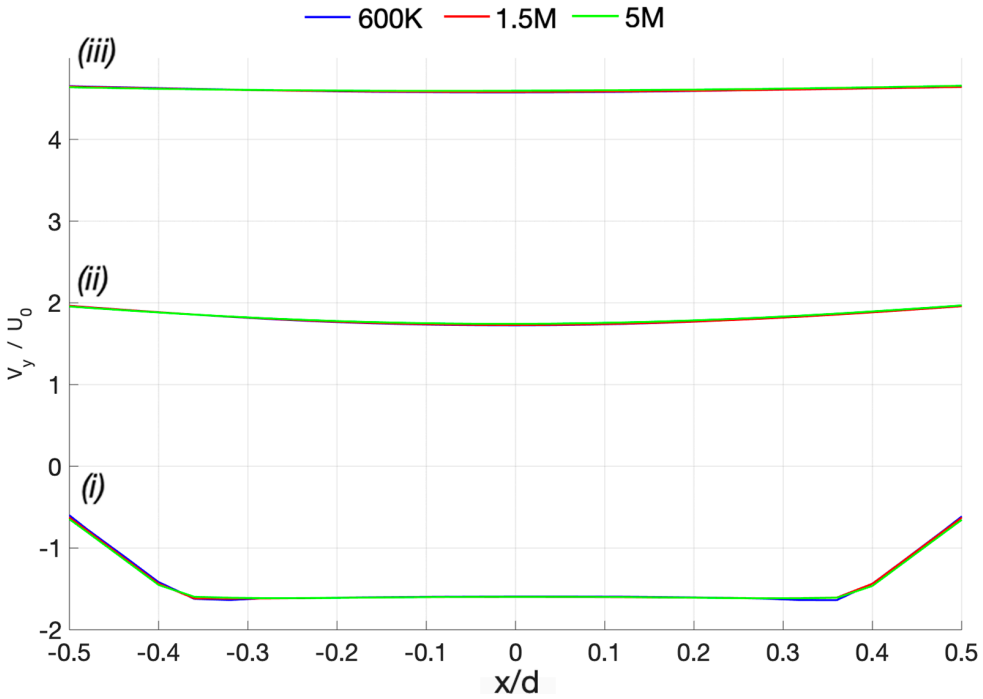

FIGURE 3.9: Cross-stream distributions of phase-averaged stream-wise V_y/U_0 velocity during the maximum ingestion phase comparing the 600,000 CV mesh, the 1.5 million CV mesh and the 5 million CV mesh for Case 2 at stations *(i)* $y/d = 0$, *(ii)* 0.5 and *(iii)* 1.

Figure 3.9 shows the same three stations studied in Figure 3.7 of the phase-averaged stream-wise V_y/U_0 velocity profiles but during the maximum ingestion phase for Case 2. All meshes studied are compared in this plot: the 600,00 CV mesh (blue), the 1.5 million CV mesh (red) and the 5 million CV mesh (green). Velocity profiles *ii* and *iii* show that the curves from the three simulations are almost identical. Both profiles show a central region where the small and intermediate mesh underpredict slightly the results obtained from the

5 million CV mesh simulation. Finally, it is possible to observe that the first profile presents a close match between all meshes, particularly in the region $-0.3 < x/d < 0.3$.

Having analyzed the velocity profiles from the three meshes studied, the conclusion extracted from the mesh and grid sensitivity analysis section is that the difference in the results obtained between the 600,000 CV mesh and the 1.5 million CV mesh is not substantial. The 5 million CV mesh has been estimated, on average, as 1.74% more accurate than the 1.5 million CV mesh. The mesh chosen to analyze its results during Chapter 4 of the thesis is the 1.5 million CV mesh. It allows to compute better results than the 600,000 CV mesh. Although the 5 million CV mesh gives more precise outcomes, the computational time and resources needed are substantially greater than for the 1.5 million CV mesh. The resources needed are out of this project's scope. The 5 million CV mesh was performed only for 5 cycles, compared to the 20 employed for the intermediate mesh. Therefore, more cycles may be needed in order to obtain a better representation of the flow. Moreover, one run of the 5 million CV mesh takes several days to be performed and it is, thus, out of the scope of this work.

4. Results Discussion

The results from the numerical simulations that have been performed for this work are presented in this chapter.

This chapter firstly introduces the vortex pair dynamics using phase-averaged span-wise vorticity plots. The next step is to analyze the behavior of the flow using time-averaged and phase-averaged velocity streamlines. Inside this section, there are also comparisons between the two jet formation criteria analyzed in this work. The next section explains the near field flow of the jet with the help of cross-stream phase-averaged stream-wise V_y/U_0 velocity profiles. Inside this section, there are comparisons between the maximum expulsion phase and the maximum ingestion phase, apart from comparisons between the two different jet formation criteria used in this work. Finally, the jet half-width is presented for both JFC studied in this work.

4.1 Synthetic Jet Dynamics

The behavior of the vortex pair formed at the orifice exit during the expulsion phase and of the vortex pair formed inside the cavity during the ingestion phase is analyzed in this section. The phase-averaged span-wise vorticity is examined in eight characteristic instants in order to explain the vortex dynamics of a synthetic jet actuator. Two different cases have been used: the $JFC = 3$ case and the $JFC = 6$ case . Both cases are used to explain the vortex dynamics and a comparison between both is also undertaken.

Figure 4.1 and Figure 4.2 show the phase-averaged span-wise vorticity for the $JFC = 3$ case and the $JFC = 6$ during eight different phases of the cycle ((a) $\phi = 0^\circ$ (b) $\phi = 45^\circ$ (c) $\phi = 90^\circ$ (d) $\phi = 135^\circ$ (e) $\phi = 180^\circ$ (f) $\phi = 225^\circ$ (g) $\phi = 270^\circ$ and (h) $\phi = 315^\circ$). The cycle is split in two figures for ease of comparison. It is important to note that the membrane shape has been modeled as a sinusoidal function of the membrane radius, as in Miró *et al.* [5] and Xia and Qin [7]. Since the membrane shape is modeled with a sine function, the maximum expulsion phase is located at $\phi = 0^\circ$ (where the velocity in the y coordinate is the maximum) and the maximum ingestion phase is located at $\phi = 180^\circ$ (where the velocity in the y coordinate is the minimum). Moreover, the membrane positive maximum deflection is located at $\phi = 90^\circ$ and the membrane negative maximum deflection is located at $\phi = 270^\circ$. Figure 4.1a shows the maximum expulsion instant ($\phi = 0^\circ$). At this point, the

vortex pair has accumulated enough vorticity to detach from the bottom wall, located at $y/d = 0$, and starts to advect downstream. Figure 4.1b presents the same instant for the $JFC = 6$ case and it is possible to observe that the size of the coherent structure is bigger than in the $JFC = 3$ case. In addition, the center of the coherent structure is located at $y/d = 3$ for Figure 4.1b whereas for Figure 4.1a is found below $y/d = 2$. In Figure 4.1c it is possible to observe that the vortex pair has moved downstream and it is further away from the jet orifice, with both centers located at $y/d = 3.0$ approximately. Figure 4.1d shows a notable difference between both cases: the structure is beginning to lose its coherence and to transition into turbulence without detaching, which is not happening in Figure 4.1c. The following plots (Figure 4.1e and Figure 4.1f) show the instant when the ingestion cycle begins ($\phi = 90°$). It is also noteworthy that the vortex pair is completely detached from the jet orifice in Figure 4.1e, with the center at $y/d = 4$, whereas in Figure 4.1f the pair of vortices has almost dissipated and its center is located above $y/d = 6$. Furthermore, both structures are too far to be affected by the suction during the ingestion phase. Figure 4.1g reveals that the vortex pair has mixed significantly with ambient fluid and has begun to dissipate whereas in the $JFC = 6$ case (see Figure 4.1h) the coherent structure has essentially dissipated. Moreover, the shear layers which connected both vortices to the jet orifice have completely vanished for both cases. It is also important to note that the formation of the other vortex pair has already started inside the cavity. The maximum ingestion phase ($\phi = 180°$) is represented in Figure 4.2a and Figure 4.2b. It is possible to observe that the vortex pair has grown in size due to the roll-up process and is beginning to detach from the wall inside the cavity, for the $JFC = 3$ case, and the vortex pair is starting to impinge the bottom wall, for the $JFC = 6$ case. The coherent structure has the center located at $y/d = -2$, in Figure 4.2a, and at $y/d = -3$ for the Figure 4.2b. In both cases the former pair of vortices at the exit has dissipated sufficiently, thus allowing the jet to be formed. In Figure 4.2c, it is possible to observe that the vortex pair formed inside the cavity has advected downstream and has impinged the bottom wall. The vortex pair at the exit is even more difficult to notice than before, in Figures 4.2c and 4.2d.

Figure 4.2e and 4.2f represent the end of the ingestion phase and the start of the expulsion phase, where $\phi = 270°$. After impinging the bottom wall, the vortical structure inside the cavity is starting to lose its coherence and to dissipate in Figure 4.2f. For the $JFC = 3$ case, in Figure 4.2e, the pair of vortices is still impinging the bottom wall inside the cavity.

In the exit of both plots, the vortex pair starts the roll-up process, being formed at the lips of the orifice, where it starts to emerge from the fluid and begins to grow in size.
The roll-up process continues, in Figure 4.2g and Figure 4.2h, until it reaches its maximum width (approximately the orifice width in this case) at the maximum expulsion phase, and the process starts again. Both figures also show the last remnants of the pair of vortices formed at the exit during the previous cycle.

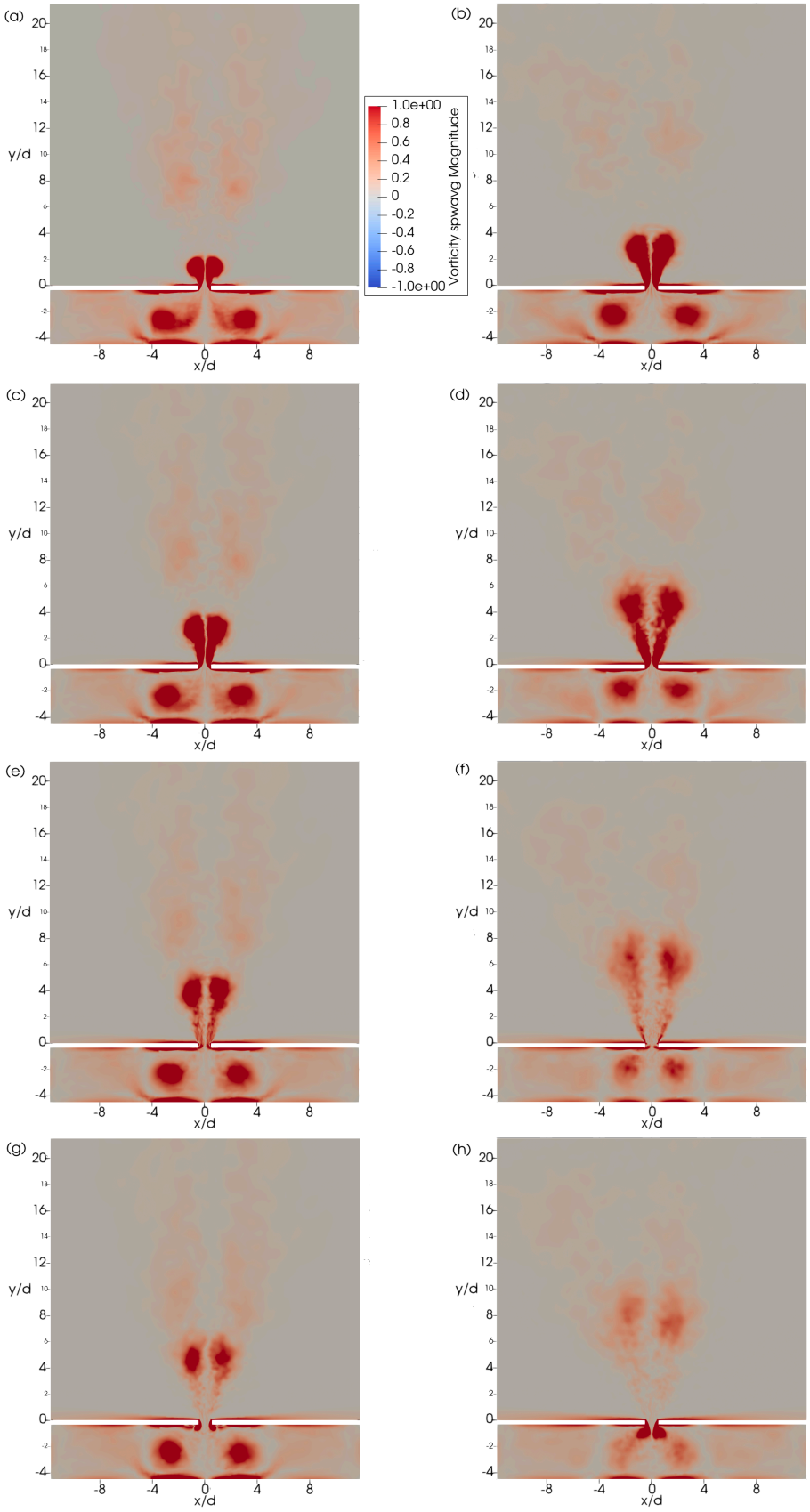

FIGURE 4.1 : Phase-averaged span-wise vorticity for the $JFC = 3$ case (left column) and the $JFC = 6$ case (right column) at four instants of the first half of the cycle: (a) and (b) $\phi = 0^{\circ}$ (c) and (d) $\phi = 45^{\circ}$ (e) and (f) $\phi = 90^{\circ}$ (g) and (h) $\phi = 135^{\circ}$.

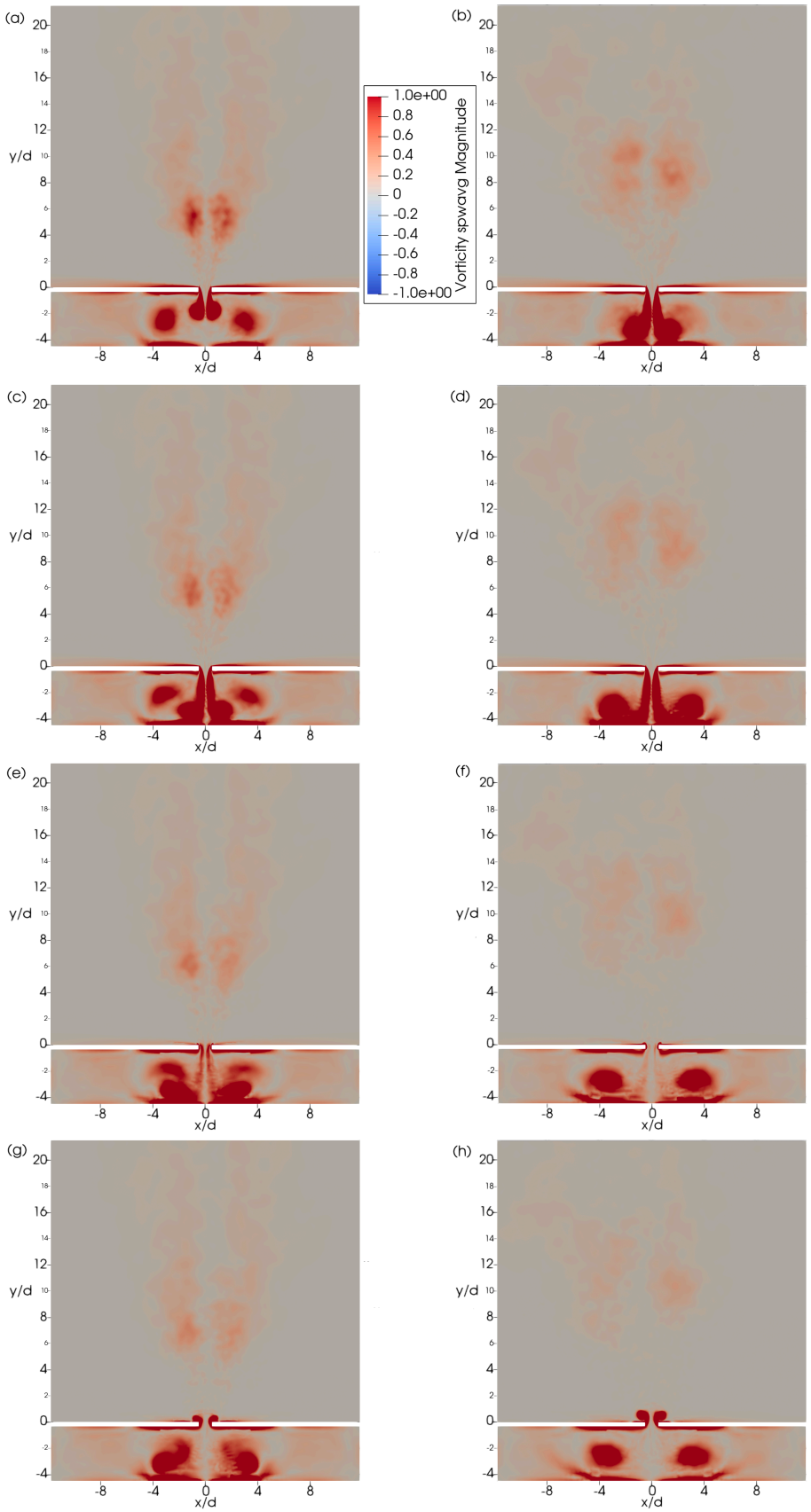

FIGURE 4.2 : Phase-averaged span-wise vorticity for the $JFC = 3$ case (left column) and the $JFC = 6$ case (right column) at four instants of the second half of the cycle: (a) and (b) $\phi = 180°$ (c) and (d) $\phi = 225°$ (e) and (f) $\phi = 270°$ (g) and (h) $\phi = 315°$.

4.2 Flow Topology

A good way to understand the topology of the flow and study its characteristics is by the use of streamlines. The time-averaged span-wise velocity streamlines from both jet formation criteria cases studied are used in this section to explain the flow topology. Turbulent kinetic energy extracted from both cases is also shown.

4.2.1 Time-averaged Velocity Streamlines

In this section, there is an analysis of the streamlines comparing both jet formation criteria in order to understand how this parameter affects the behavior of a synthetic jet. Time-averaged span-wise velocity streamlines are used in order to explore the mean flow. It is important to note that the mean streamline time-averaged velocity plots which are used in this section are just an average of the whole fluid movement and, therefore, do not represent any particular instant of the flow motion.

Figure 4.3 shows the time-averaged span-wise velocity field for $JFC = 3$ (left) and $JFC = 6$ (right). It is possible to observe that there are two big recirculation zones for each case. There is a big mass of fluid at the jet centerline which is accelerated by the periodic motion of the membrane or diaphragm. Such mass of fluid is moved out of the domain and, by continuity, this flux needs to return back to this domain. The way to comply with this condition is by naturally forming these recirculation zones.

The time-averaged span-wise velocity streamlines in both plots die at the exit of the orifice, as it can be seen in Figure 4.3. This region, located between $y/d = 0$ and $y/d = 5$, corresponds to the maximum vortex pair which is advecting downstream. When this maximum pair of vortices disappears, approximately at $y/d = 3.5$, jet creation begins and, hence, the time-averaged span-wise velocity streamlines start to be formed. The reason why streamlines cannot merge within this region is because it is the vortex pair area and jet formation has not yet begun.

For the $JFC = 3$ case, the jet centerline of the time-averaged span-wise velocity streamlines is straight whereas for the $JFC = 6$ case the jet centerline is more curved. Such phenomenon is due to the fact that a bigger JFC implies more linear momentum delivered into the exit medium, which contributes to bigger recirculation zones and a sloppier jet centerline. Another notable difference when examining Figure 4.3 is that the center of both

recirculation zones for the $JFC = 3$ case is found between $y/d = 50$ and $y/d = 55$ while in the $JFC = 6$ case they are located at $y/d = 35$, approximately. This difference can be due to the jet formation criteria again, because in the $JFC = 6$ more linear momentum is provided and allows the recirculation zones to be formed and to be dragged upstream faster.

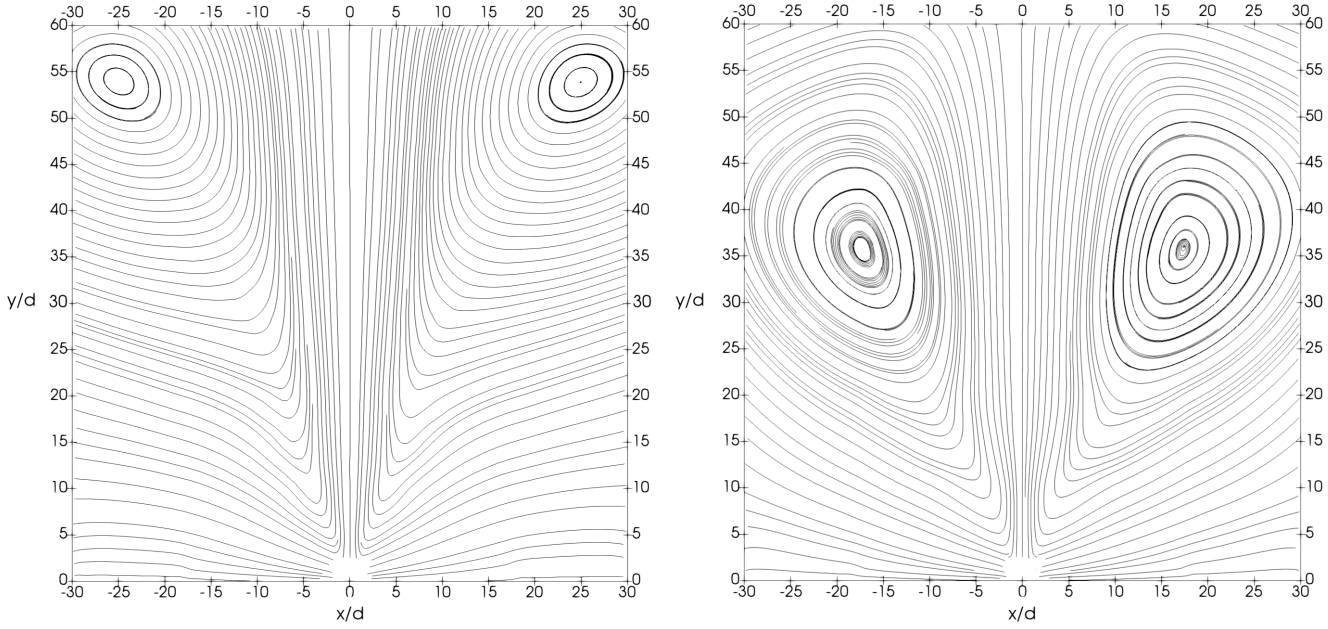

FIGURE 4.3 : Streamlines corresponding to time-averaged span-wise velocity fields comparing the $JFC = 3$ case (left) and the $JFC = 6$ case (right).

4.2.2 Turbulent Kinetic Energy

In order to analyze the flow topology, it is also interesting to compute the turbulent kinetic energy of the flow field. Such parameter is used in this section and compared between both jet formation criteria studied.

Figure 4.4 presents the time-averaged span-wise spatial distribution of the turbulent kinetic energy $\overline{k}$ for the $JFC = 3$ case (left) and for the $JFC = 6$ case (right). The turbulent kinetic energy is defined as the trace of the Reynolds stress tensor divided by two, as shown in the following equation:

$$\overline{k} = \frac{1}{2}\overline{u_i' u_i'} \tag{4.1}$$

where u_i' is defined as $u_i' = u_i - \overline{u_i}$ and the overline operator ($\bar{\cdot}$) denotes that the magnitude has been averaged in time.

The jets formed in both cases are clearly turbulent since they are formed in the orifice lips. Transition into turbulence starts at the orifice, where secondary structures break the vortices during the roll-up process [13]. The formation phenomenon looks quite similar for both cases in Figure 4.4, with the formation maximum located at $y/d = 2$. From this point upwards, the turbulent kinetic energy $\overline{k}$ transition gradient from the $JFC = 6$ case is much bigger than its counterpart allowing such case to arrive up to $y/d = 8$ whereas for the $JFC = 3$ it only reaches $y/d = 6$. The reason on such difference is the fact that the vortex pair from the $JFC = 6$ case is able to reach a higher y/d in Figure 4.1 compared to the smaller JFC case. There is also a notable difference inside the cavity between both cases. The energy is transported downstream, reaching $y/d = -2$ for the $JFC = 6$ case whereas for the smaller JFC case the energy is not transported lower than $y/d = 1.5$. The $JFC = 6$ case shows values of the 0.2 region of turbulent kinetic energy that the $JFC = 3$ case does not have. Moreover, there is more turbulent kinetic energy $\overline{k}$ transported inside the cavity, by the effect of the recirculation zones, in the bigger jet formation criteria case than in the smaller one, due to the fact that with a greater JFC more linear momentum is applied.

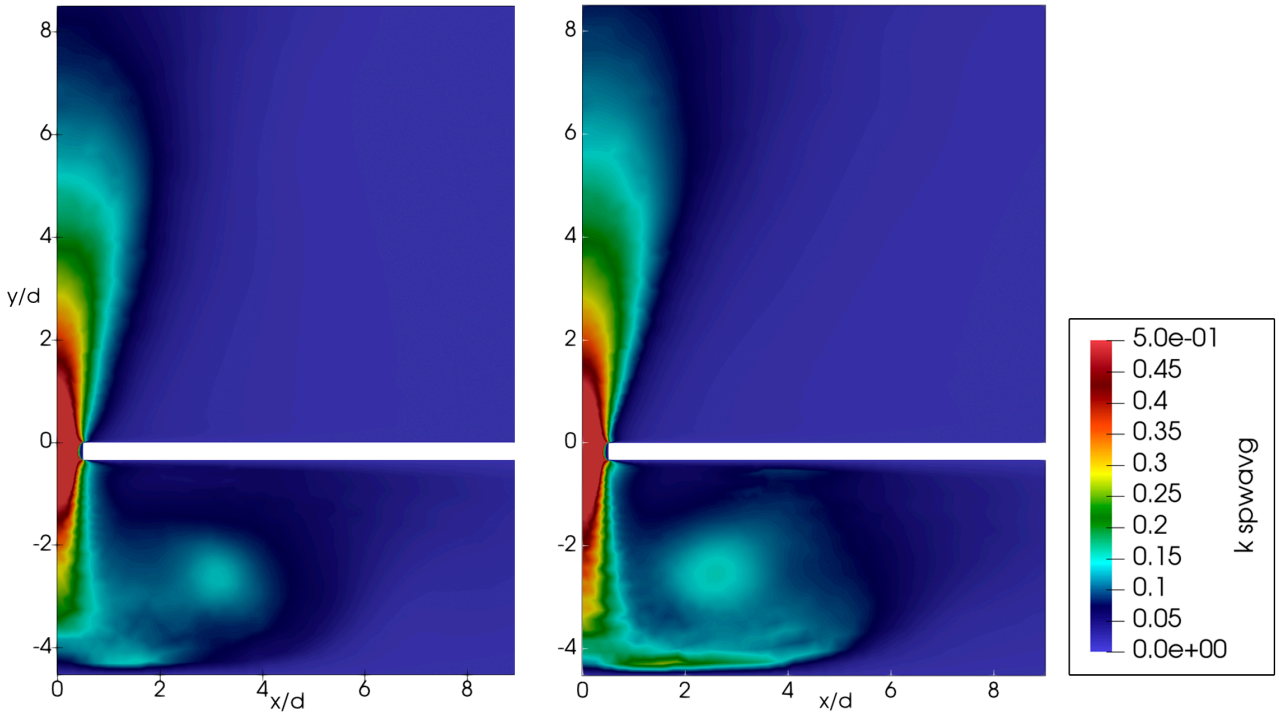

FIGURE 4.4 : Distribution of the time-averaged span-wise turbulent kinetic energy $\overline{k}$ comparing the $JFC = 3$ case (left) and the $JFC = 6$ case (right).

4.3 Near Field Jet Flow

In order to understand the behavior of the jet flow in the surroundings of the orifice, the profiles of the cross-stream phase-averaged stream-wise V_y/U_0 velocity at different stations have been extracted and studied. There is also a comparison between JFC throughout this section in order to understand its behavior.

Figure 4.5 presents the cross-stream distributions of phase-averaged stream-wise V_y/U_0 velocity during the maximum expulsion phase ($\phi = 0°$) at eleven different stations for both jet formation criteria used in this work. The first distinct region which can be seen in the first three stations of the $JFC = 3$ case and in stations *i, ii, iii , iv* and *v* of the $JFC = 6$ case is the orifice length. The orifice length is located in the $-0.5 < x/d < 0.5$ zone in the first profile from both cases, as it is expected. The fluid which has been expelled from the jet orifice is contained inside this area. The region between $-0.25 < x/d < 0.25$ in the first plot of Figure 4.5 is known as the potential core and it is the zone where the velocity deficit is very low. The velocity deficit is defined as $U_\infty - u_1(x)$, where U_∞ is the velocity at the jet centerline and $u_1(x)$ is the stream-wise velocity distribution within the wake and, in this case, it is used to study the penetration of the jet. Moving up the stations, increasing the y coordinate, it is possible to observe that jet penetration grows due to the fact that the velocity deficit increases. From a certain point onwards (station *v* for the $JFC = 3$ case) the velocity deficit begins to diminish, and, hence, does jet penetration. Until a certain point, at station *vii* for the $JFC = 3$ case, from which there is almost no jet penetration. This has implications on the jet width, as it is further seen.

It is possible to see in Figure 4.5 that there is a difference in the jet penetration between both jet formation criteria studied. Under this formulation, a bigger JFC implies there is a greater deflection of the membrane (or diaphragm) inside the actuator cavity. Such greater deflection allows to move a bigger mass of ambient fluid downstream and, therefore, to deliver more linear momentum into the external medium. The velocity deficit starts to increase at $y/d = 0$ for both cases until station *v* ($y/d = 2$) for the $JFC = 3$ case and station *viii* ($y/d = 3.5$) for the $JFC = 6$ case where it begins to decrease. At station *vii* ($y/d = 3$) for the $JFC = 3$ case and at station *xi* ($y/d = 5$) for the $JFC = 6$ case, the velocity deficit is very low and, hence, there is almost no jet penetration. If Figure 4.1 is further examined, it is possible to see that the vortex pair coalescence begins at a higher y/d for the $JFC = 6$ case than for the $JFC = 3$ which implies that jet formation occurs

higher for the $JFC = 6$ case. Vortex coalescence starting higher for the $JFC = 6$ case means the velocity deficit is bigger and takes more time to be reduced, hence jet penetration is dragged for more y/d and jet formation occurs at a higher station than for the smaller jet formation criteria used.

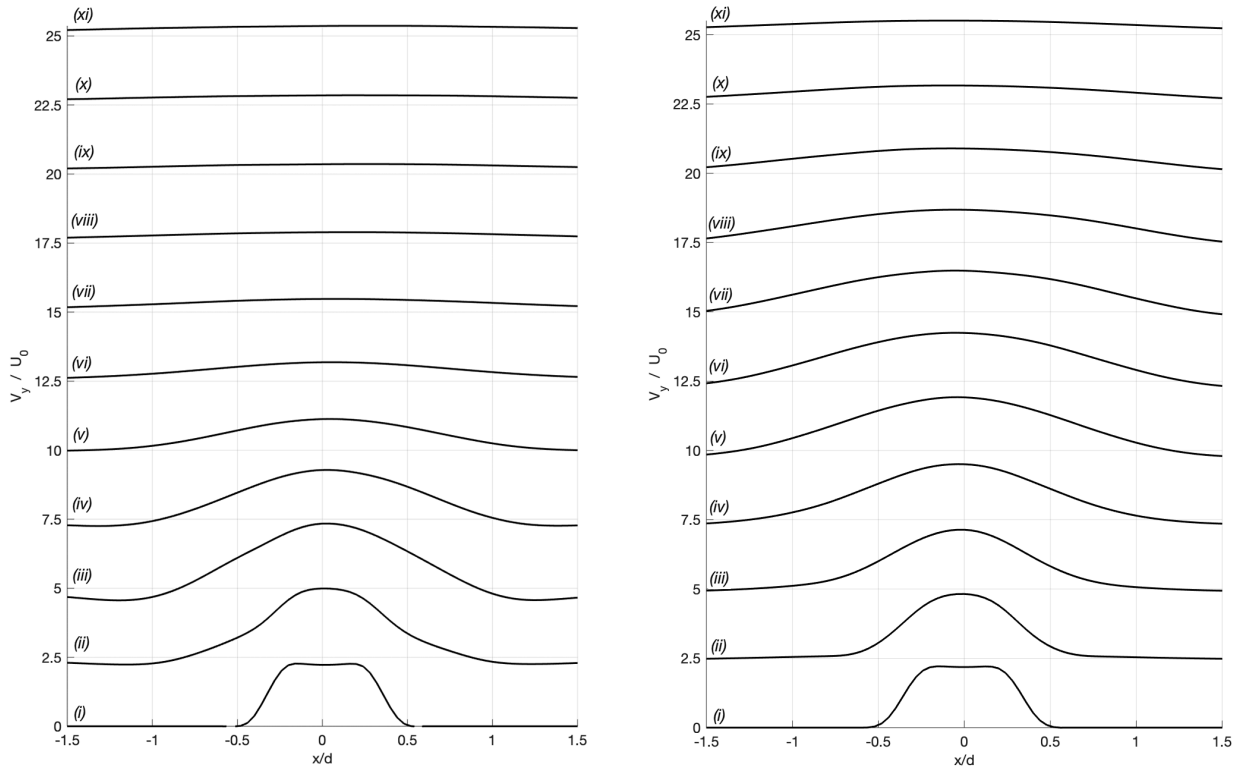

FIGURE 4.5 : Cross-stream distributions of phase-averaged stream-wise V_y/U_0 velocity during the maximum expulsion phase ($\phi = 0°$) for $JFC = 3$ (left) and for $JFC = 6$ (right) at stream-wise stations *(i)* $y/d = 0.0$, *(ii)* 0.5, *(iii)* 1.0, *(iv)* 1.5, *(v)* 2.0, *(vi)* 2.5, *(vii)* 3.0, *(viii)* 3.5, *(ix)* 4.0, *(x)* 4.5 and *(xi)* 5.0.

Figure 4.6 presents the cross-stream distributions of phase-averaged stream-wise V_y/U_0 velocity during the maximum ingestion phase ($\phi = 180°$) at eleven different stations for both jet formation criteria studied. As it happened in the maximum expulsion phase, the first y/d station (but also the second one in this case) is the same for both JFC. Such phenomenon is analyzed in Figure 4.8. The orifice length is represented in this figure in the $-0.5 < x/d < 0.5$ area, as in the former case. The potential core area is wider than in the ingestion case, located approximately at $-0.35 < x/d < 0.35$. The flow pattern is the same: the velocity deficit grows as the y coordinate increases, therefore jet penetration decreases due to being in the suction phase. The only notable difference in Figure 4.6 is the

penetration effect on stations *ix*, *x* and *xi* from the $JFC = 3$ case. Such phenomenon is produced by the fact that the velocity deficit grows and, hence, jet penetration increases along the y axis. Stations *ix*, *x* and *xi* ($y/d = 4$, 4.5 and 5, respectively) from the $JFC = 3$ case represent the stationary jet. It can not be seen in the $JFC = 6$ case from Figure 4.6 because such phenomenon occurs at a higher y/d station. Consequently, Figure 4.7 has been extracted in order to explain this phenomenon for both jet formation criteria cases analyzed.

Figure 4.7 shows the cross-stream distributions of phase-averaged stream-wise V_y/U_0 velocity during the maximum ingestion phase ($\phi = 180°$) at stations $y/d = 4$, 4.5 and 5 for the $JFC = 3$ case whereas for the bigger jet formation criteria stations $y/d = 8$, 9 and 10 are represented. These particular stations have been chosen due to the fact that it is the moment where it is possible to observe the stationary jet in both cases. The velocity deficit increases along with the y coordinate up to the point, represented in Figure 4.7, where jet penetration is clear. The reason why such phenomenon occurs at stations $y/d = 8$, 9 and 10 for the $JFC = 6$ case compared to stations $y/d = 4$, 4.5 and 5 for the $JFC = 3$ case is because the bigger jet formation criteria permits a bigger membrane deflection which imparts more linear momentum into the system and results in more fluid movement downstream. The capture area within the $JFC = 6$ case is, therefore, bigger than in the $JFC = 3$ case.

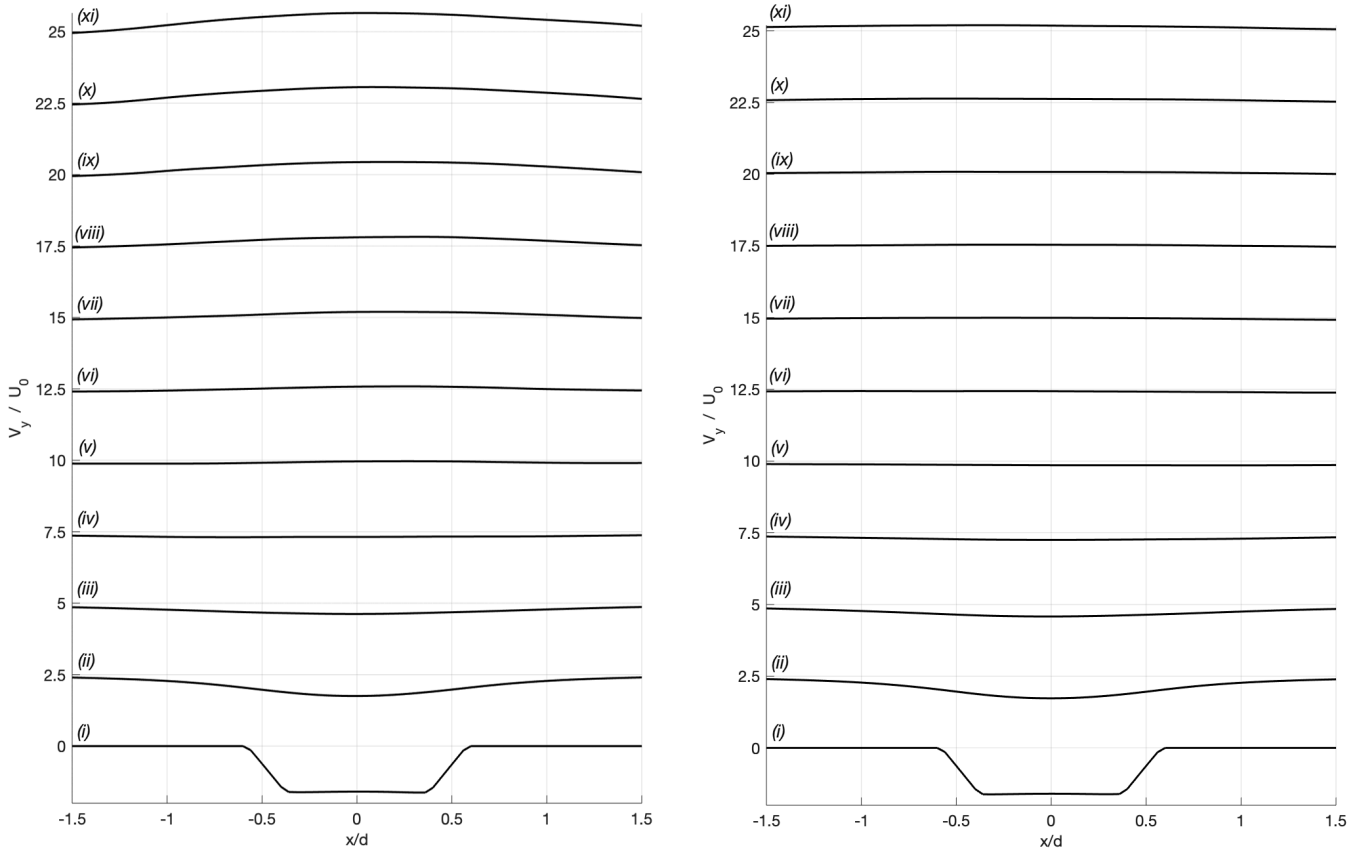

FIGURE 4.6 : Cross-stream distributions of phase-averaged stream-wise V_y/U_0 velocity during the maximum ingestion phase ($\phi = 180°$) for $JFC = 3$ (left) and for $JFC = 6$ (right) at stream-wise stations *(i)* $y/d = 0.0$, *(ii)* 0.5, *(iii)* 1.0, *(iv)* 1.5, *(v)* 2.0, *(vi)* 2.5, *(vii)* 3.0, *(viii)* 3.5, *(ix)* 4.0, *(x)* 4.5 and *(xi)* 5.0.

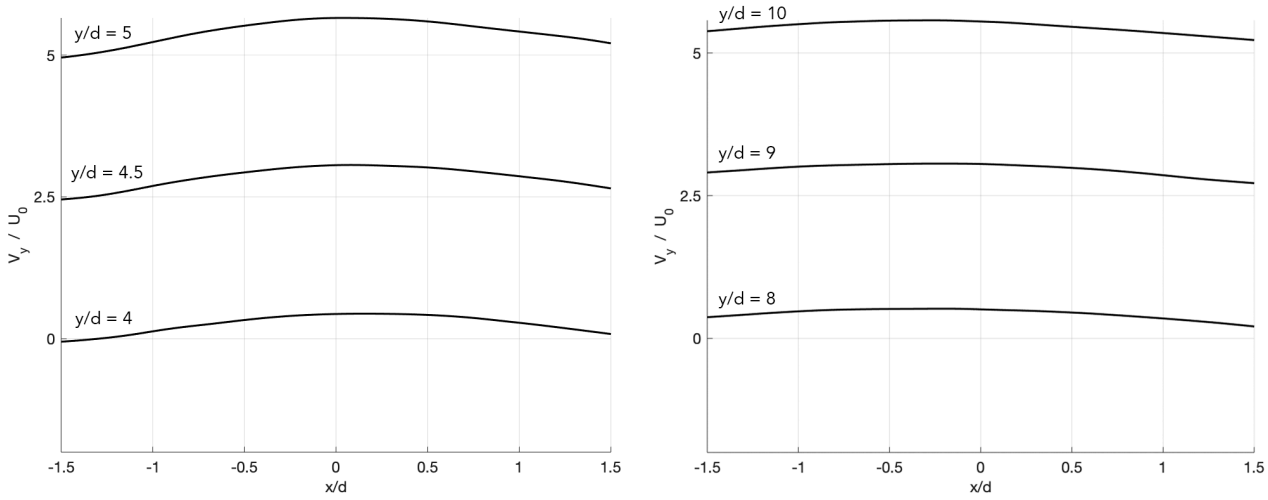

FIGURE 4.7 : Cross-stream distributions of phase-averaged stream-wise V_y/U_0 velocity during the maximum ingestion phase ($\phi = 180°$) at stream-wise stations $y/d = 4.0$, 4.5, 5.0 for $JFC = 3$ (left) and at stream-wise stations $y/d = 8.0$, 9.0, 10.0 for $JFC = 6$ (right).

Earlier in this section, it has been pointed out that the first profile, corresponding to $y/d = 0$, looks almost identical in both cases for both maximum expulsion and maximum ingestion phase. Figure 4.8 presents the comparison between both jet formation criteria for the cross-stream distributions of phase-averaged stream-wise V_y/U_0 velocity during the maximum ingestion phase (left) and the maximum ingestion phase (right). The only station analyzed is the first one, $y/d = 0$, in the region $-0.5 < x/d < 0.5$. Such area of study has been earlier identified as the orifice length region, for the maximum expulsion phase graph. If the left plot from Figure 4.8 is closely examined, the $JFC = 3$ potential core area is marginally wider than the $JFC = 6$ case. Aside from that, both profiles look almost identical. If the graph which represents the maximum ingestion cycle in Figure 4.8 is carefully analyzed, the difference between both jet formation criteria is almost unnoticeable.

The conclusion extracted from the study of Figure 4.8 leads to believe that both expulsion and suction phase dynamics are independent of the JFC value. It is also noteworthy that a bigger JFC does not affect significantly the vicinity of the orifice but, instead, its effect is more notable further away in the domain. Miró *et al.* [22] studied the phase and span-wise averaged velocity and temperature profiles at the actuator orifice for different values of the Reynolds number: $Re = 50$, 100, 300, 500 and 1000 for the slotted configuration. The conclusion extracted from his study is that there is almost no difference between the different profiles throughout the five different Re numbers studied for both ingestion and suction. This results lead to believe that the ingestion and expulsion dynamics from a SJA are independent of the Reynolds number.

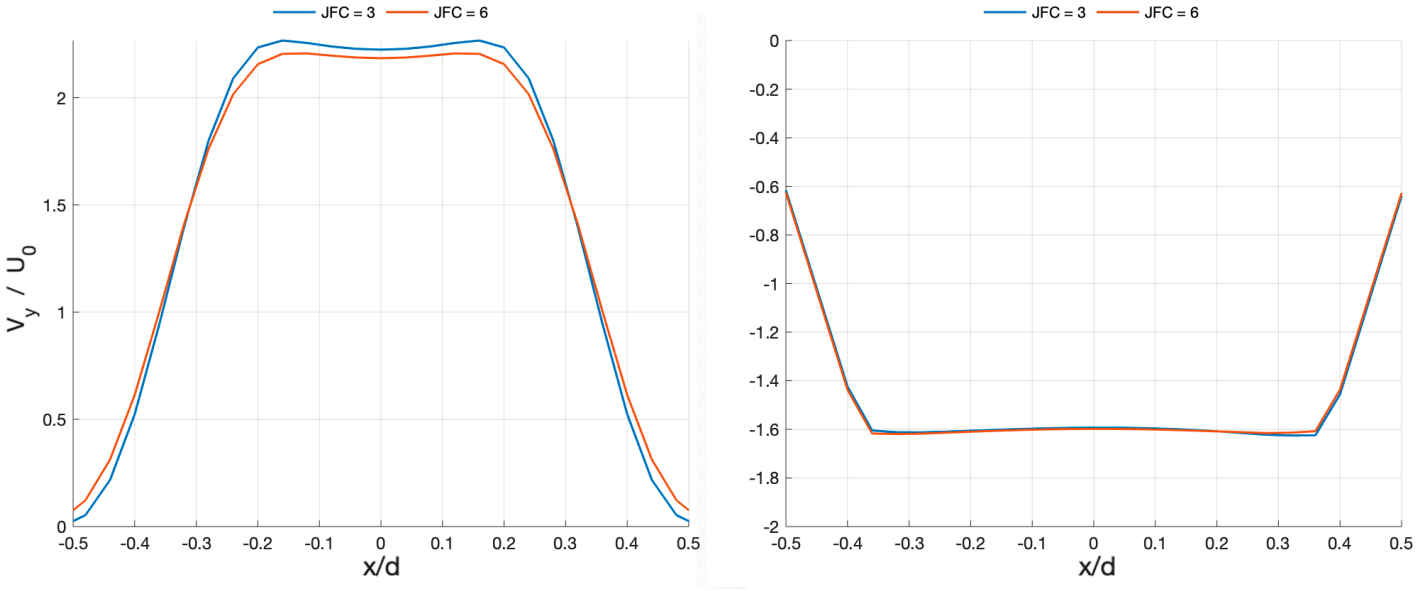

FIGURE 4.8 : Cross-stream distributions of phase-averaged stream-wise V_y/U_0 velocity during the maximum expulsion phase (left) and during the maximum ingestion phase (right) at stream-wise station $y/d = 0$ for both JFC studied.

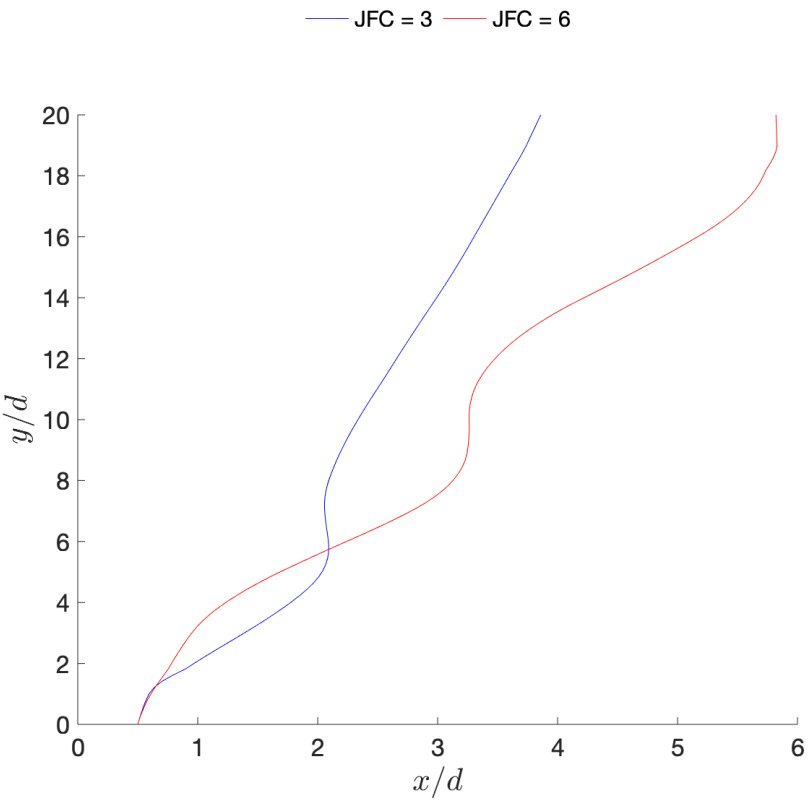

FIGURE 4.9 : Jet half-width with the domain height for both JFC studied.

Figure 4.9 shows the jet half-width with the domain height for both jet formation criteria analyzed in this study. The jet half-width is defined as the distance from the centerline where the velocity deficit has decayed down to a half of its maximum value [5, 22]. It can be seen that both jet formation criteria cases start in the same x/d and follow the same trend up to $y/d = 0.6$, approximately, due to the effect of the potential core. Moving away from the orifice, the velocity deficit begins to increase differently for both cases due to the JFC parameter, which governs how much jet formation occurs. The jet half-width from the $JFC = 3$ case is wider until $x/d = 2$ because the pair of vortices, as seen in Figure 4.1, has the center located at a lower y/d compared to the $JFC = 6$, allowing jet formation to start earlier and the jet half-width to be wider at the beginning. The $JFC = 3$ case arrives up to $x/d = 4$ whereas the bigger jet formation criteria case reaches $x/d = 6$. As it can be deduced from this graph, the jet is wider as the JFC increases. Miró *et al.* [22] also demonstrates that the jet widens as Reynolds number increases.

Conclusion

The behavior of a slotted synthetic jet actuator (SJA) discharging into an external quiescent medium has been studied. Three different mesh densities have been evaluated for the case of study: the first with 600,000 CV, the second with 1.5 million CV and the third with 5 million CV. The velocity profiles have been studied in order to analyze which mesh density suits better the scope of this work. Both the 600,000 CV mesh and the 1.5 million CV mesh underpredict the results of the 5 million CV mesh for the majority of the outcomes studied. The 1.5 million CV mesh has been proved as a decent improvement over the 600,000 CV mesh. The 5 million CV mesh provides, on average, a 1.74% improvement in accuracy over the 1.5 million CV. The final mesh used to extract the results has been the 1.5 million CV mesh, due to being the best compromise between precision and computational cost.

Two different cases have been considered for the numerical simulations: Case 1 with $JFC = 3$, and Case 2 with $JFC = 6$. The hypothesis of incompressible regime has been taken into account due to the fact that the ratio between the actuator driving frequency and the Helmholtz frequency complies with the condition $f_0 \,/\, f_h < 0.5$ for both JFC studied. The membrane movement has been taken into consideration using ALE formulation modeled as a sinusoidal function of the membrane radius. The ratio between the height of the cavity and the orifice exit diameter has been set to $\delta c/B = 0.15$ for $JFC = 6$, taking into account earlier studies. Therefore, issues when using the ALE model for the membrane motion have been avoided. Furthermore, $\delta c/B$ set to 0.15 leaves room to increase the JFC for future studies. Large Eddy Simulations (LESs) have been carried out in order to perform the numerical simulation using the Wall-Adapting Local Eddy-viscosity (WALE) closure for the sub-grid scale (SGS) terms.

Regarding the flow dynamics, it has been seen that a pair of vortices is formed during the expulsion phase at the orifice lips. The pair rolls-up and starts to advect downstream until the vortices lose their coherence and begin to coalesce into a net jet able to transfer momentum to the external fluid. Notable differences have been found between the two cases analyzed, in particular, the vortices in Case 2 ($JFC = 6$) reach $y/d = 6$ before dissipating into the jet. In contrast, in Case 1 the vortex pair only reaches $y/d = 4$. The ingestion phase also features the vortex pair which impinges the bottom wall of the cavity

The time-averaged velocity streamlines show two recirculation zones. The membrane oscillation produces a volume change which allows the fluid to be expelled from the orifice and, by continuity, returns back into the cavity which is the explanation of the formation of these recirculation zones. The velocity streamlines do not merge at the exit of the orifice because it is the zone where the vortex pair is located. When the pair of vortices disappears, jet formation begins.

The formation phenomenon of the turbulent kinetic energy until $y/d = 2$ looks quite similar in both cases studied. Nevertheless, the turbulent kinetic energy transition gradient is much bigger for Case 2, reaching $y/d = 8$, compared to Case 1, which only arrives up to $y/d = 6$. It is again related with the height at which the vortex pair is able to reach.

The phase-averaged stream-wise velocity profiles for the expulsion phase show the potential core for both cases is very similar. The bigger JFC corresponds to a greater deflection of the actuator membrane. Therefore, more fluid can be dragged downstream, increasing the linear momentum of the system. The result is a lower penetration in the y/d coordinate for Case 1 compared to Case 2. The potential core during the ingestion phase is very much similar between the cases analyzed. The stationary jet appears at $y/d = 4 - 5$ for Case 1 and at $y/d = 8 - 10$ for Case 2.

The jet half-width and the velocity profiles demonstrate that both potential cores are almost identical. Therefore, the expulsion and ingestion dynamics seem to be independent from the JFC and Re number, as seen in the literature for the latter. Furthermore, the fact that the jet half-width is wider at low x/d for Case 1 means the jet is formed earlier than in Case 2. Moreover, the jet half-width is overall wider for Case 2 compared to Case 1, which leads to believe that the jet gets wider as the JFC increases.

Future Work

This work has studied synthetic jets in the slotted configuration. A first future work can be to perform the same analysis on the axisymmetric configuration. Two main cases have been considered, in order to study the behavior of the jet formation criteria. Lower and higher values of the JFC could also be studied (e.g. $JFC = 2$ or $JFC = 9$), as well as different Reynolds numbers, e.g., between $Re = 50$ to $Re = 1000$. More cycles for the 5 million CV mesh could also be computed in the future to obtain a better approximation of the flow for the simulations studied.

The present study could also be the starting point of a more complex project, such as an AFC device. The advantage of this work in order to be implemented in a future AFC device is the fact that this study has used a SJA that discharges without an actual medium. Therefore, parameters such as penetration of the jet or the exit velocity, with its corresponding profile, can be calculated in order to model better an AFC case.

Bibliography

[1] B. L. Smith and A. Glezer. The Formation and Evolution of Synthetic Jets. *Physics of Fluids*, Vol. 10, No. 9, pp. 2281–2297, 1998.

[2] J. E. Cater and J. Soria. The Evolution of Round Zero-Net-Mass-Flux Jets. *Journal of Fluid Mechanics*, Vol. 472, pp. 167–200, 2002.

[3] R. Holman, Y. Utturkar, R. Mittal, B. L. Smith, and L. N. Cattafesta III. Formation Criterion for Synthetic Jets. *AIAA Journal*, Vol. 43, No. 10, pp. 2110–2116, 2005.

[4] Y.D. Afanasyev. Formation of Vortex Dipoles. *Physics of Fluids*, Vol. 18, No. 3, pp. 1–9, 2006.

[5] A. Miró. Flow and Heat Transfer of Impinging Synthetic Jets. *Universitat Politècnica de Catalunya*, Terrassa, 2019.

[6] A. Polsenberg, M. Milano, M. G. G'Sell, K. Fischer, J. Burdik. Synthetic jet propulsion for small underwater vehicles. *Proceedings of the 2005 IEEE International Conference on Robotics and Automation*, pp. 182-188, Barcelona, 2005.

[7] H. Xia and N. Qin. Dynamic Grid and Unsteady Boundary Conditions for Synthetic Jets Flow. Presented at *Aerospace Sciences Meeting and Exhibit, 43rd*, pp. 1-9, 2005.

[8] Q. Gallas. On the Modeling and Design of Zero-Net Mass Flux Actuators. *PhD thesis*, University of Florida, 2005.

[9] D. B. Goldstein and C. Y. Lee. Two-Dimensional Synthetic Jet Simulation. *AIIA Journal*, Vol. 40, No. 3, 2003.

[10] R. Mittal, R. Rampunggoon and H. S. Udaykumar. Interaction of a Synthetic Jet with a Flat Plate Boundary Layer. *AIAA Paper* 2773, 2001.

[11] Y. Utturkar, R. Holman, R. Mittal, B. Carroll, M. Sheplak and L. Cattafesta. A Jet Formation Criterion for Synthetic Jet Actuators. *AIAA Paper* 0636, 2003.

[12] M. A. Feero, P. Lavoie, and P. E. Sullivan. Influence of Cavity Shape on Synthetic Jet Performance. *Sensors and Actuators, A: Physical*, Vol. 223, pp. 1–10, 2015.

[13] R. B. Kotapati, Mittal, and L. N. Cattafesta III. Numerical study of a transitional synthetic jet in quiescent external flow. *Journal of Fluid Mechanics*, Vol. 581, pp. 287–321, 2007.

[14] C. S. Yao, F. J. Chen, D. Neuhart, and J. Harris. Synthetic Jets in Quiescent Air. *In Proc. NASA LaRC Workshop on CFD Validation of Synthetic Jets and Turbulent Separation Control*, Williamsburg, 2004.

[15] P. Spalart, L. Hedges, M. Shur and A. Travin. Simulation of Active Flow Control on a Stalled Airfoil. *Flow, Turbulence and Combustion*, Vol. 71, No. 1-4, pp. 361–373, 2003.

[16] A. Tuck and J. Soria. Active Flow Control over a NACA 0015 Airfoil using a ZNMF Jet. Presented at *Australasian Fluid Mechanics Conference*, *15th, Sydney*, 2004.

[17] D. C. McCormick. Boundary Layer Separation Control With Directed Synthetic Jets. Presented at *Aerospace Science Meeting and Exhibit*, *38th, Reno*, *AIAA Pap.* 0519, 2000.

[18] I. Rodriguez, O. Lehmkuhl, R. Borell. Effects of the Actuation on the Boundary Layer of an Airfoil at Reynolds Number $Re = 60000$. *Flow, Turbulence and Combustion*, 2020.

[19] A. Arshad, M. Jabbal, Y. Yan. Synthetic Jet Actuators For Heat Transfer Enhancement - A Critical Review. *International Journal of Heat and Mass Transfer,* Vol 146, No. 118815, 2020.

[20] Y. H. Liu, S. Y. Tsai and C. C. Wang. Effect of Driven Frequency on Flow and Heat Transfer of an Impinging Synthetic Air Jet. *Applied Thermal Engineering*, Vol. 75, pp. 289–297, 2015.

[21] B. Smith and G. Swift. Synthetic Jets at Large Reynolds Number and Comparison to Continuous Jets. Presented at *AIAA Computational Fluid Dynamics Conference*, *15th*, Vol 2001-3030, pp. 20, 2001.

[22] A. Miró, M. Soria, J.C. Cajas and I. Rodríguez. Numerical Study of Heat Transfer from a Synthetic Impinging Jet with a Detailed Model of the Actuator Membrane. *International Journal of Thermal Sciences,* Vol 136, pp. 287-298, 2019.

[23] BSC-CNS. Alya Multiphysics Code. http://www.bsc.es/computer-applications/alya-system, 2014. Checked on: 26/06/2020.

[24] A. Miró, M. Soria, C. Moulinec, J. C. Cajas, Y. Fournier. Numerical Investigations on Rectangular and Circular Synthetic Jet Impingement. *Tenth International Conference on Computational Fluid Dynamics (ICCFD10).* Barcelona, 2018.

[25] M. Gul, O. Uzol and I. S. Akmandor. An Experimental Study on Active Flow Control Using Synthetic Jet Actuators over S809 Airfoil. *Journal of Physics*: Conference Series 524 012101, 2014.

[26] Barcelona Supercomputing Center. Alya - High Performance Computational Mechanics. https://www.bsc.es/research-development/research-areas/engineering-simulations/alya-high-performance-computational Checked on: 20/06/2020.